Supporting Information

Heteroatom-Doped Carbon Electrocatalysts Derived from Nanoporous Two-Dimensional Covalent Organic Frameworks for Oxygen Reduction and Hydrogen Evolution

Chao Yang, [†,◊] Shanshan Tao, [§] Ning Huang, [‖] Xiaobin Zhang, [‡] Jingui Duan, [*,#] Rie Makiura, [*,⊥] and Shinya Maenosono [*,†]

[†]*School of Materials Science, Japan Advanced Institute of Science and Technology, 1-1 Asahidai, Nomi, Ishikawa 923-1292, Japan*

[§]*Department of Chemistry, Faculty of Science, National University of Singapore, 3 Science Drive 3, Singapore 117543, Singapore*

[‖]*MOE Key Laboratory of Macromolecular Synthesis and Functionalization, Department of Polymer Science and Engineering, Zhejiang University, Hangzhou 310027, China*

[‡]*Center for Nano Materials and Technology, Japan Advanced Institute of Science and Technology, 1-1 Asahidai, Nomi, Ishikawa 923-1292, Japan*

[#]*State Key Laboratory of Materials-Oriented Chemical Engineering, College of Chemical Engineering, Nanjing Tech University, Nanjing 211816, China*

[⊥]*Department of Materials Science, Graduate School of Engineering, Osaka Prefecture University, 1-2 Gakuen-cho, Naka-ku, Sakai, Osaka 599-8570, Japan*

Corresponding Authors

*E-mail: duanjingui@njtech.edu.cn; r-makiura@mtr.osakafu-u.ac.jp; shinya@jaist.ac.jp.

Present Addresses

[◊]*School of Chemistry and Chemical Engineering, State Key Laboratory of Metal Matrix Composites, Shanghai Jiao Tong University, Shanghai 200240, China*

Materials and methods

Section S1. Monomer synthesis

1,3,6,8-tetrakis(4-aminophenyl)pyrene (TAP) [1,2]

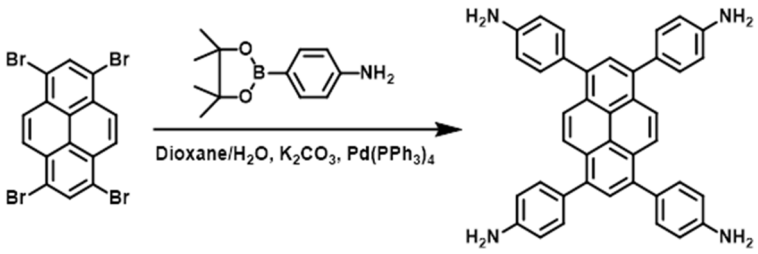

1,3,6,8-tetrabromopyrene (2.0 g, 3.86 mmol), 4-(4,4,5,5-tetramethyl-1,3,2-dioxaborolan-2-yl)aniline (3.8 g, 17.4 mmol), K_2CO_3 (2.9 g, 21.2 mmol), and $Pd(PPh_3)_4$ (445 mg, 0.39 mmol) were added to dioxane/H_2O (5:1 v/v, 42 mL) and heated to reflux for 3 days. After cooling to room temperature, H_2O (50 mL) was added. The resulting precipitate was collected *via* filtration and washed with H_2O and methanol. Recrystallization was from dioxane, followed by drying under high vacuum to yield **TAP** (1.97 g, 90%) as a yellow solid. ^{1}H NMR (400 MHz, DMSO-d_6) δ: 8.13 (s, 4H), 7.79 (s, 2H), 7.36, 7.34 (d, J=8.3 Hz, 8H), 6.78, 6.76 (d, J=8.3 Hz, 8H), 5.32 (s, 8H).

1,2,4,5-tetrakis(4-aminophenyl)benzene (TAB) [3]

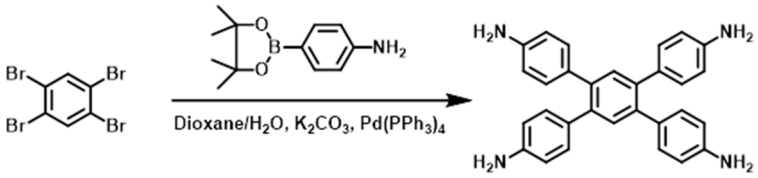

1,2,4,5-tetrabromobenzene (1.5 g, 3.8 mmol), 4-(4,4,5,5-tetramethyl-1,3,2-dioxaborolan-2-yl)aniline (3.7 g, 17.1 mmol), K_2CO_3 (2.1 g, 15.7 mmol), and $Pd(PPh_3)_4$ (439 mg, 0.38 mmol) were added to dioxane/H_2O (5:1, v/v, 36 mL) and heated to reflux for 3 days. After cooling to room temperature, H_2O (50 mL) was added. The resulting precipitate was collected *via* filtration and washed with H_2O and methanol. Recrystallization was from dioxane, followed by drying under high vacuum to yield **TAB** (1.8 g, 90%) as a gray solid. ^{1}H NMR (400 MHz, $CDCl_3$) δ: 7.39 (s, 2H), 7.04, 7.02 (d, J=8.5 Hz, 8H), 6.58, 6.56 (d, J=8.1 Hz, 8H).

1,2,4,5-tetrakis(4-formylphenyl)benzene (TFB) [4]

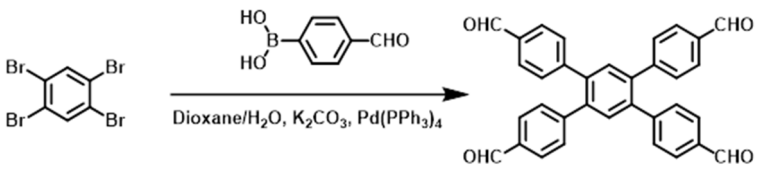

1,2,4,5-tetrabromobenzene (1.91 g, 4.84 mmol), 4-formylphenyl boronic acid (1.60 g, 10.64 mmol), K_2CO_3 (2.68 g, 19.4 mmol) and $Pd(PPh_3)_4$ (578 mg, 0.5 mmol) in dioxane/H_2O (5:1 v/v, 72 mL) were degassed and backfilled with N_2 three times.

The suspension was stirred under N_2 at 100 °C for 72 h. After cooling to room temperature, the mixture was concentrated and then extracted with EtOAc. The organic phase was dried over anhydrous $MgSO_4$ and then concentrated under reduced pressure to remove the solvent. The crude product was purified by silica gel column chromatography to yield **TFB** (1.92 g, 80%). ^{1}H NMR (400 MHz, $CDCl_3$) *δ*: 10.00 (s, 4H), 7.81, 7.79 (d, *J*=8.4 Hz, 8H), 7.60 (s, 2H), 7.40, 7.38 (d, *J*=8.2 Hz, 8H).

1,2,4,5-tetrakis(4-formylphenyl)-3,6-dimethylbenzene (TFDB) [4]

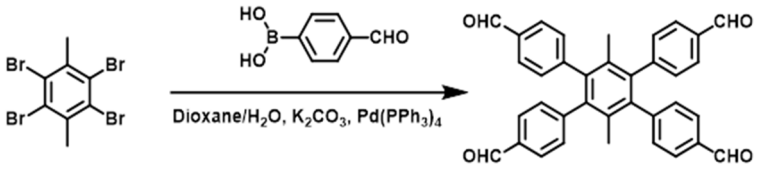

2,3,5,6-tetrabromo-*p*-xylene (2.0 g, 4.74 mmol), 4-formylphenyl boronic acid (1.56 g, 10.42 mmol), K_2CO_3 (2.62 g, 19.0 mmol) and $Pd(PPh_3)_4$ (578 mg, 0.5 mmol) in dioxane/H_2O (5:1 v/v, 66 mL) were degassed and backfilled with N_2 three times. The suspension was stirred under N_2 at 100 °C for 72 h. After cooling to room temperature, the mixture was concentrated and then extracted with EtOAc. The organic phase was dried over anhydrous $MgSO_4$ and then concentrated under reduced pressure to remove the solvent. The crude product was purified by silica gel column chromatography to afford **TFDB** (1.5 g, 60%). ^{1}H NMR (400 MHz, $CDCl_3$) *δ*: 9.91 (s, 4H), 7.72, 7.70 (d, *J*=8.3 Hz, 8H), 7.25, 7.23 (d, *J*=8.1 Hz, 8H), 1.77 (s, 6H).

Section S2. Materials characterization

Solution phase ^{1}H nuclear magnetic resonance (NMR) spectroscopy was recorded on a NMR spectrometer (Bruker Biospin Avance III, 400 MHz). Solid-state ^{13}C cross-polarization total suppression of sidebands (^{13}C CP/TOSS) and cross-polarization magic angle spinning (^{13}C CP/MAS) NMR spectra were recorded on a NMR spectrometer at a rotor frequency of 10 kHz (Bruker Biospin Avance III, 500 MHz). Fourier transform infrared (FT-IR) spectra were obtained on a infrared spectrometer (JASCO FT-IR-6100). Thermogravimetric analysis (TGA) traces were collected on a thermal gravimetric analyzer (TA Instruments TGA/SDTA851e) under N_2 atmosphere from 50 °C up to 1000 °C at a ramp rate of 5 °C min^{-1}. Solid-state ultraviolet–visible (UV-Vis) spectra were acquired on a spectrophotometer (JASCO V-780 UV-Visible/NIR).

The hypothetical modelling of 2D [4 + 4] COFs was built from a unit cell with the highest possible symmetry P2/M space group. In this way, *α* and *γ* were fixed at 90°, while *a*, *b*, *c* and *β* were free so that the building block could be slipped when refining. The A-A stacked structures were initially modelled using force-field methods and refined using density-functional tight-binding (DFTB+) methods in Materials Studio version 8.0 (Accelrys).[1,5] To monitor the modelling with different slippage degrees, *β* was adjusted in the ranges of 90° and 125° to compare these simulated patterns with that for the finally refined *β*. The A-B stacked structure of **1** was also modelled and refined by DFTB+. The structure parameters were close to those of A-A except *c*, which was almost double. However, the relative intensities were different between them because of the non-flat layer and different interlayer interaction and atomic coordination. Therefore, the simulated pattern of the A-B stacked structure looks very different from that of the A-A stacked structure and does not closely resemble the experimental data, suggesting the A-A stacking is more likely. Thus, only A-A stacked structures of **2-Me**, **3**, and **4-Me** were considered.

The geometries of TAP, TAB, TFB and TFDB were optimized by Force-field model in Materials Studio version 8.0.

The theoretical surface areas and pore sizes were simulated by Poreblazer based on refined A-A structure models of **1**, **2-Me**, **3**, and **4-Me**, respectively.

Supporting figures and tables

Section S3. FTIR spectra of 2D [4 + 4] COFs

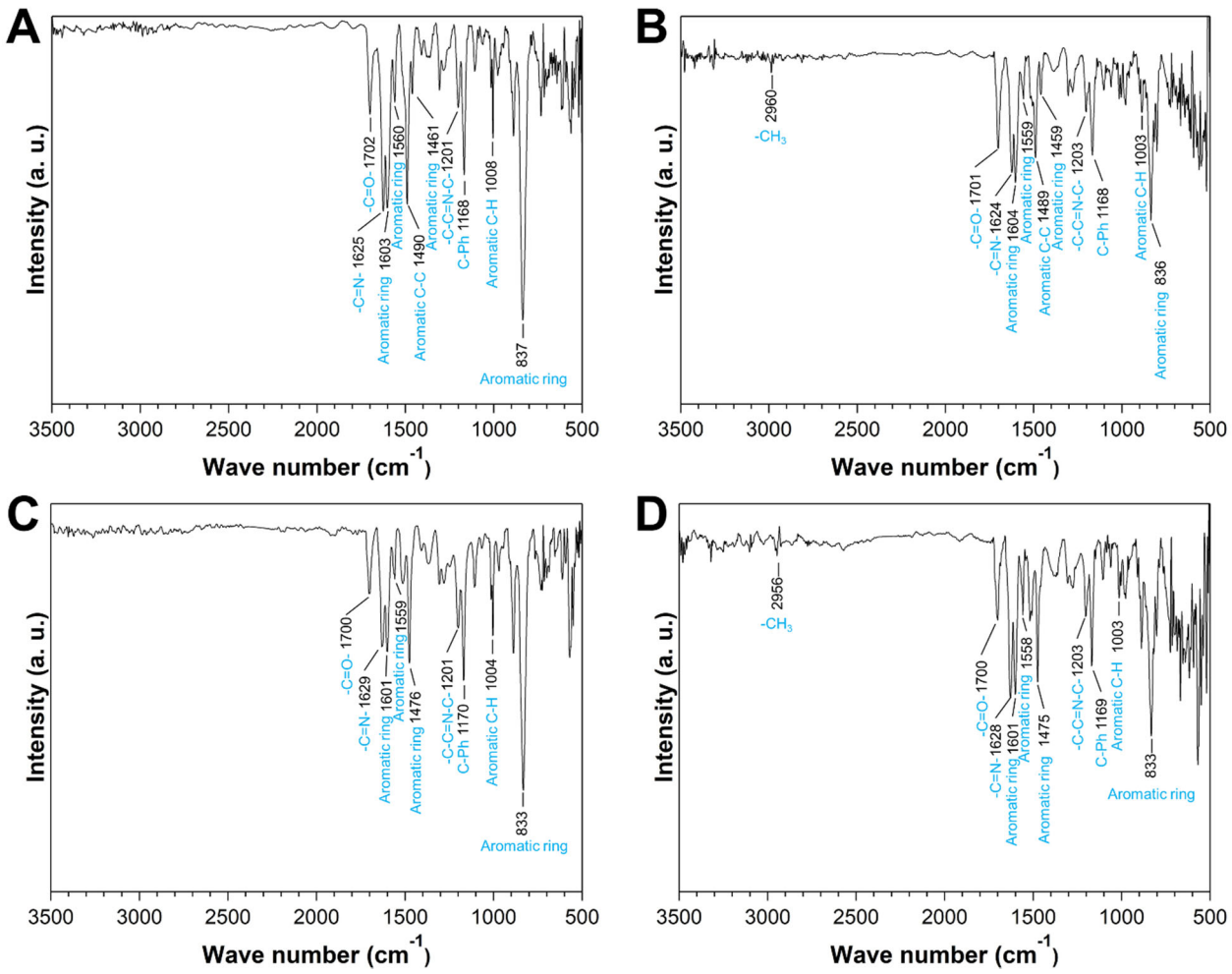

Figure S1. FTIR spectra of (A) **1**, (B) **2-Me**, (C) **3**, and (D) **4-Me**, respectively.

The formation of C=N at around 1630 cm^{-1} in FTIR spectra indicates the formation of imine bonds.

Section S4. High-resolution XPS spectra of C 1s for 2D [4 + 4] COFs

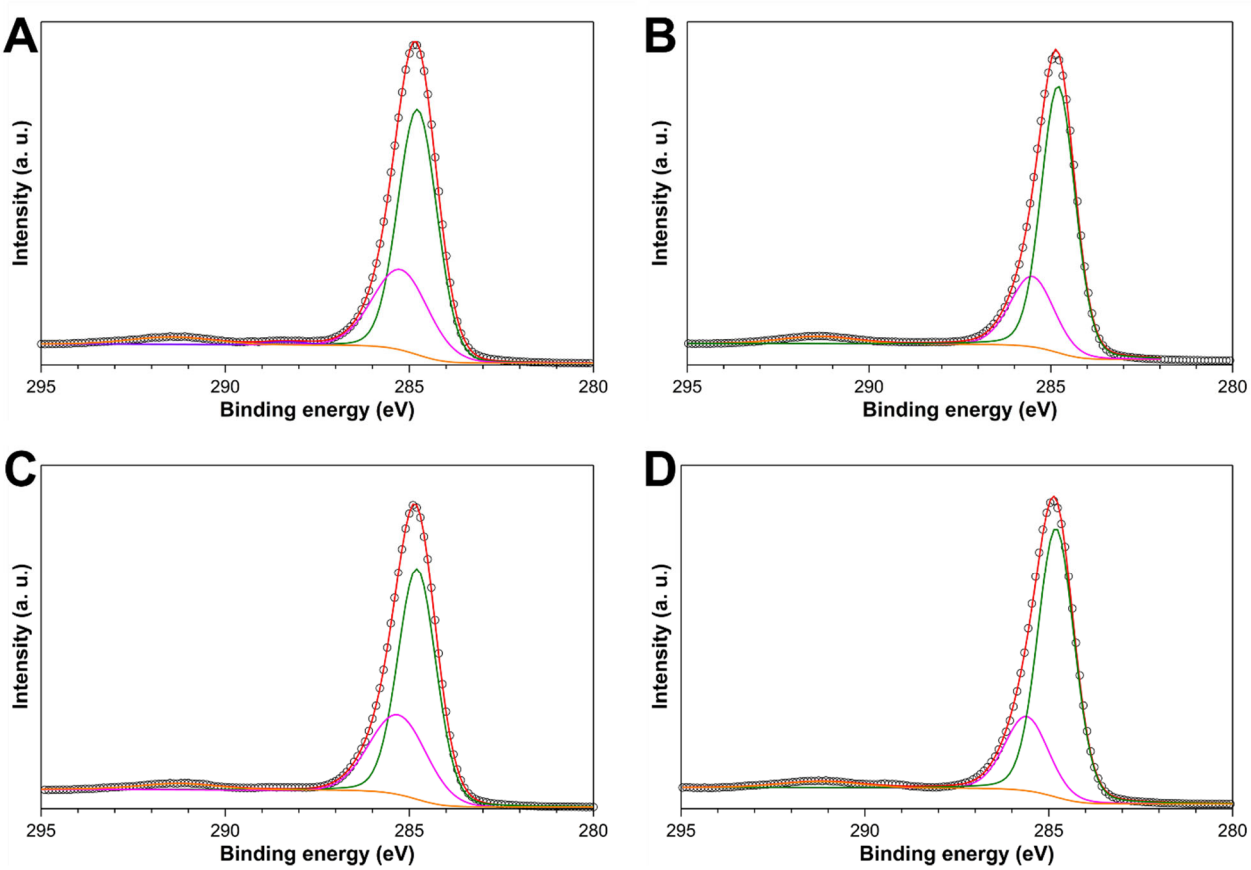

Figure S2. High-resolution XPS spectra of C 1s of (A) **1**, (B) **2-Me**, (C) **3**, and (D) **4-Me**, respectively.

C-C/C=C: 284.8 eV (green); C-N/C=N (imine bond): 285.9 eV (pink); π-π*: 291.2 eV (yellow).

The deconvoluted bands at around 285.9 eV in XPS C 1s spectra are ascribed from imine bonds in COFs.

Section S5. High-resolution XPS spectra of N 1s for 2D [4 + 4] COFs

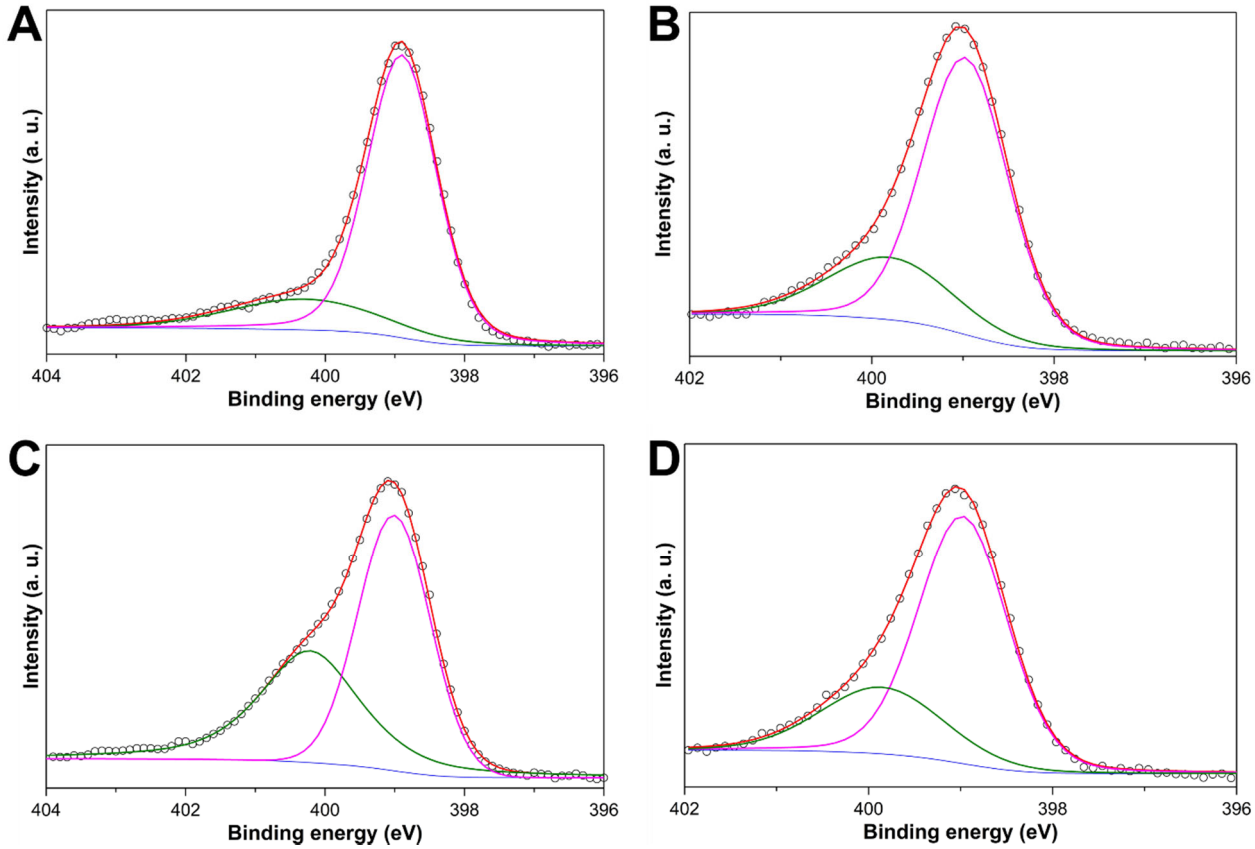

Figure S3. High-resolution XPS spectra of N 1s of (A) **1**, (B) **2-Me**, (C) **3**, and (D) **4-Me**, respectively.

C=N (imine bond): ~399.0 eV (pink); -NH_2: ~400.0 eV (green).

The deconvoluted bands at around 399.0 eV in XPS N 1s spectra are ascribed from imine bonds in COFs.

Section S6. Solid-state ^{13}C NMR spectra of 2D [4 + 4] COFs

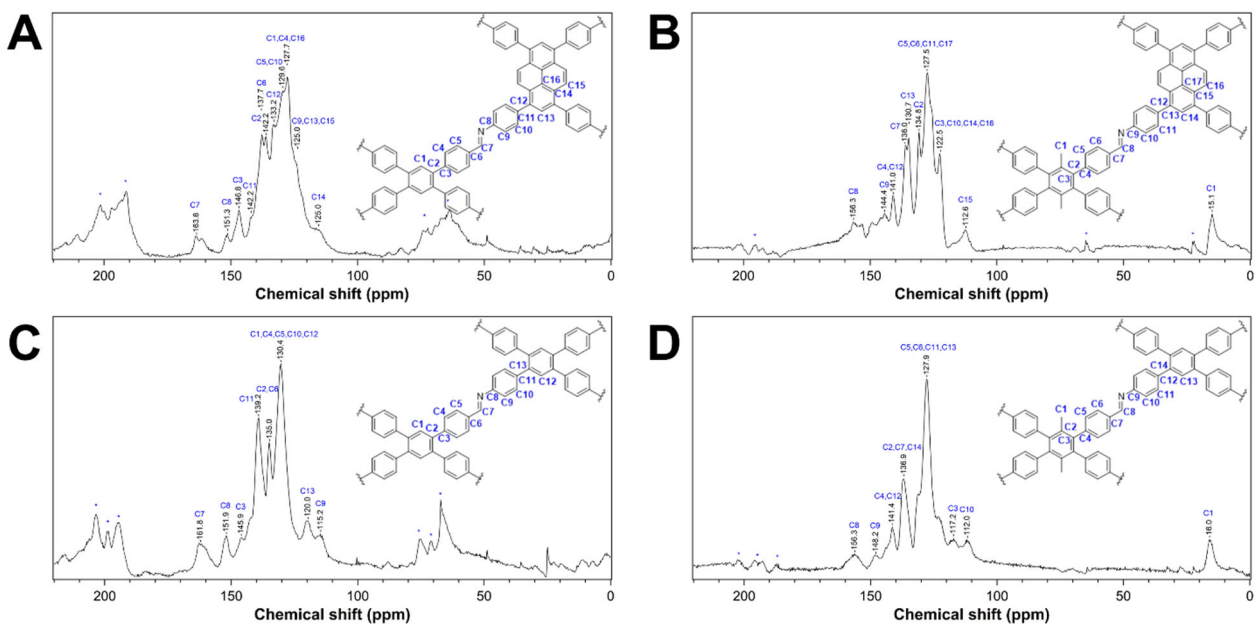

Figure S4. Solid-state ^{13}C NMR spectra of (A) **1**, (B) **2-Me**, (C) **3**, and (D) **4-Me**, respectively.

Chemical shifts at 151–156 ppm and 15.0–16.0 ppm in ^{13}C NMR spectra are assigned to imine carbon and methyl groups.

Section S7. PXRD analyses of 2D [4 + 4] COFs

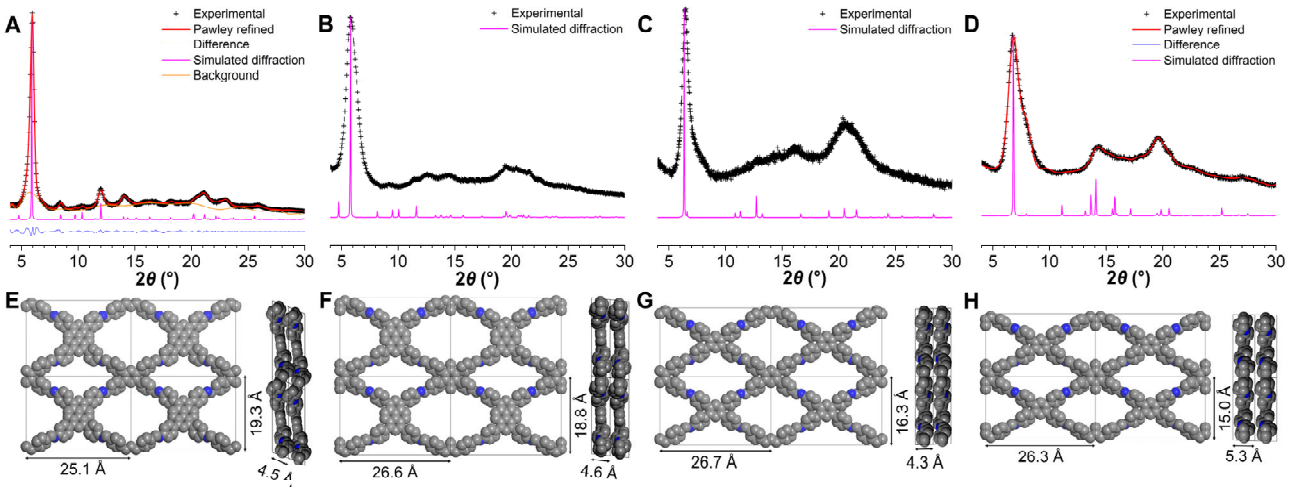

Figure S5. Experimental, Pawley-refined, and predicted PXRD patterns of A-A structures for (A) **1** (R_{wp}: 3.3%, R_p: 2.4%), (B) **2-Me**, (C) **3**, and (D) **4-Me**, respectively; Top and side view of constructed A-A structures (H is omitted for clarity) for (E) **1**, (F) **2-Me**, (G) **3**, and (H) **4-Me**, respectively.

Considering the similar P2/m topology and close crystalline sizes, four COFs all show strong diffraction peaks at 6° in PXRD patterns. Pawley refined results with smaller errors based on slipped A-A stacking structures and matched simulated diffraction peaks suggest the reasonability of structure models.

Section S8. Crystal structure analyses of 2D [4 + 4] COFs

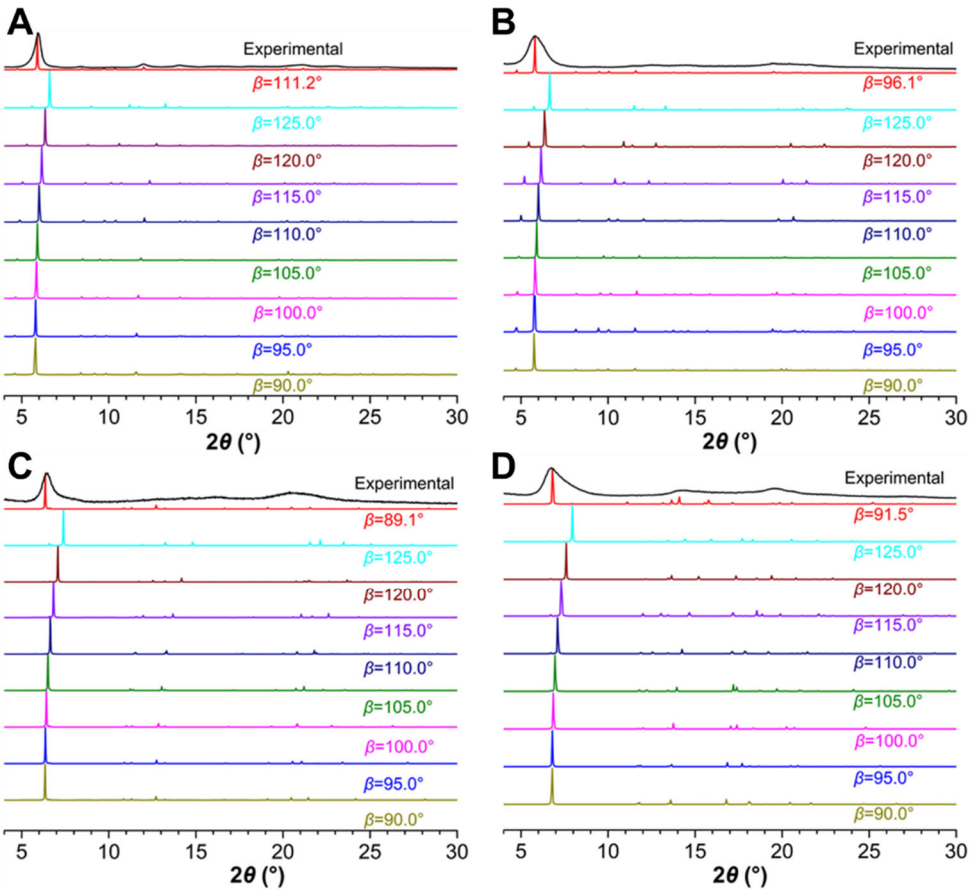

Figure S6. Simulated diffraction patterns of different slip angles (β-90°) for (A) **1**, (B) **2-Me**, (C) **3**, and (D) **4-Me**, respectively.

Considering the inclination of layers, the optimal slip angles are determined by comparing with the experimental PXRD patterns.

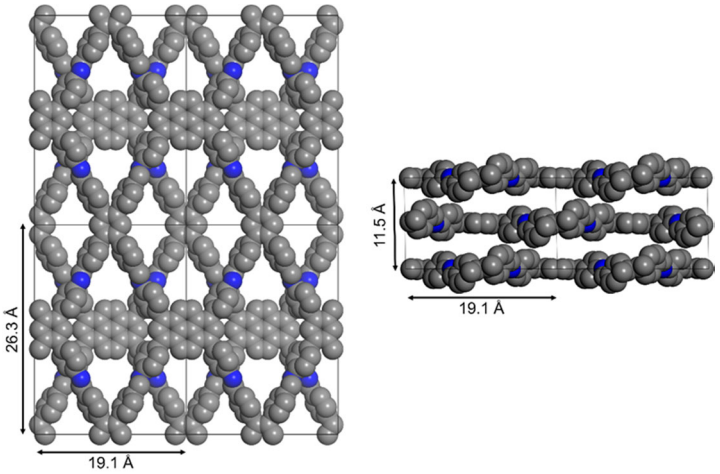

Figure S7. A-B stacked structure model (H is omitted for clarity) of **1** (top view (left), side view (right)). Symmetry: P1, a=19.1 Å, b=26.3 Å, c=11.5 Å, α=γ=90°, β=90.3°.

In order to determine stacking configurations, A-B stacked structures of **1** was built. And the simulated diffractions peaks are largely derivate the experimental, indicating the A-A stacking is more reasonable.

Section S9. Structures of building blocks

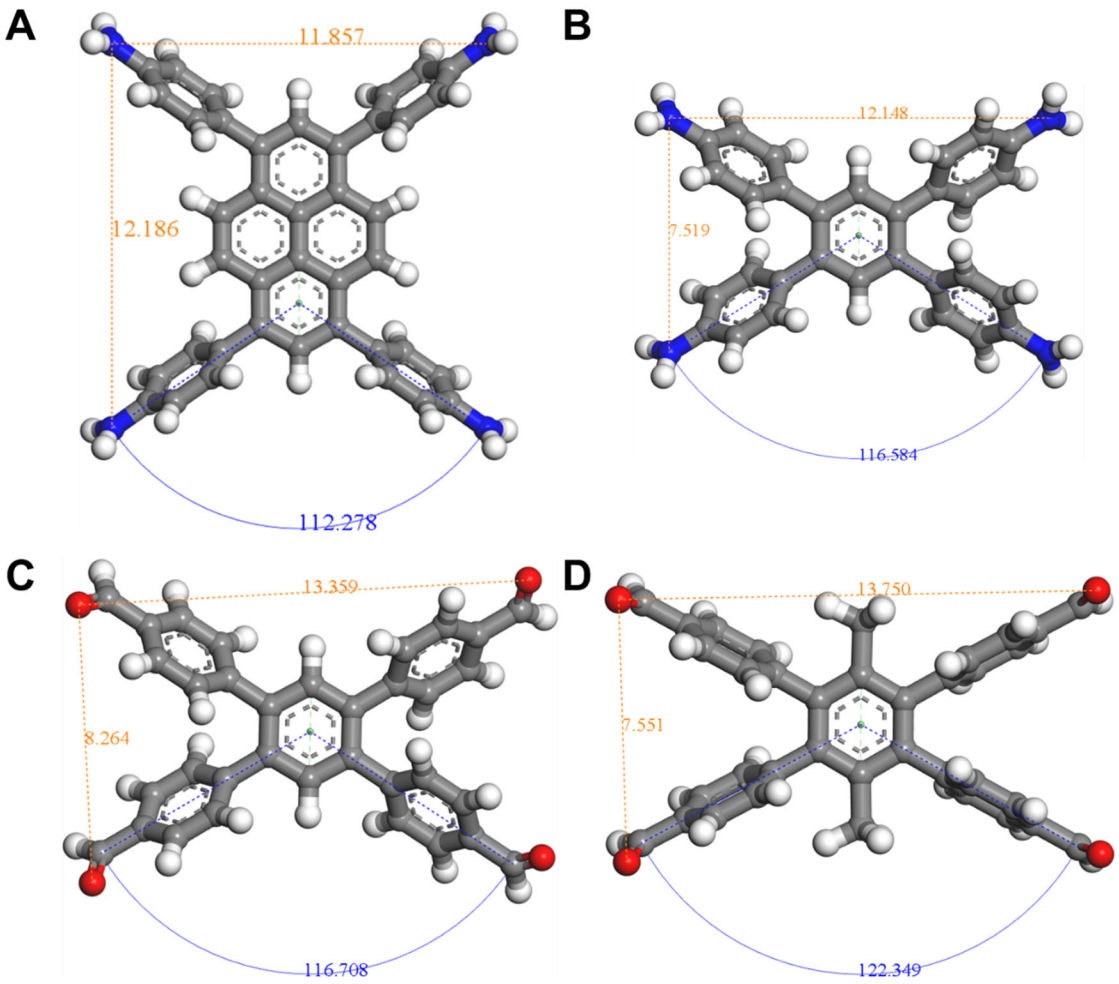

Figure S8. Structures of building blocks: (A) TAP, (B) TAB, (C) TFB, and (D) TFDB, respectively.

In the four building blocks, angles between two phenyl aldehyde groups all approximate 120° and 60°, leading to the good match between aldehyde building blocks and amino ones. In additions, the aspect ratio of TFDB is a little larger than that of TFB because of methyl groups.

Section S10. TEM images of 2D [4 + 4] COFs

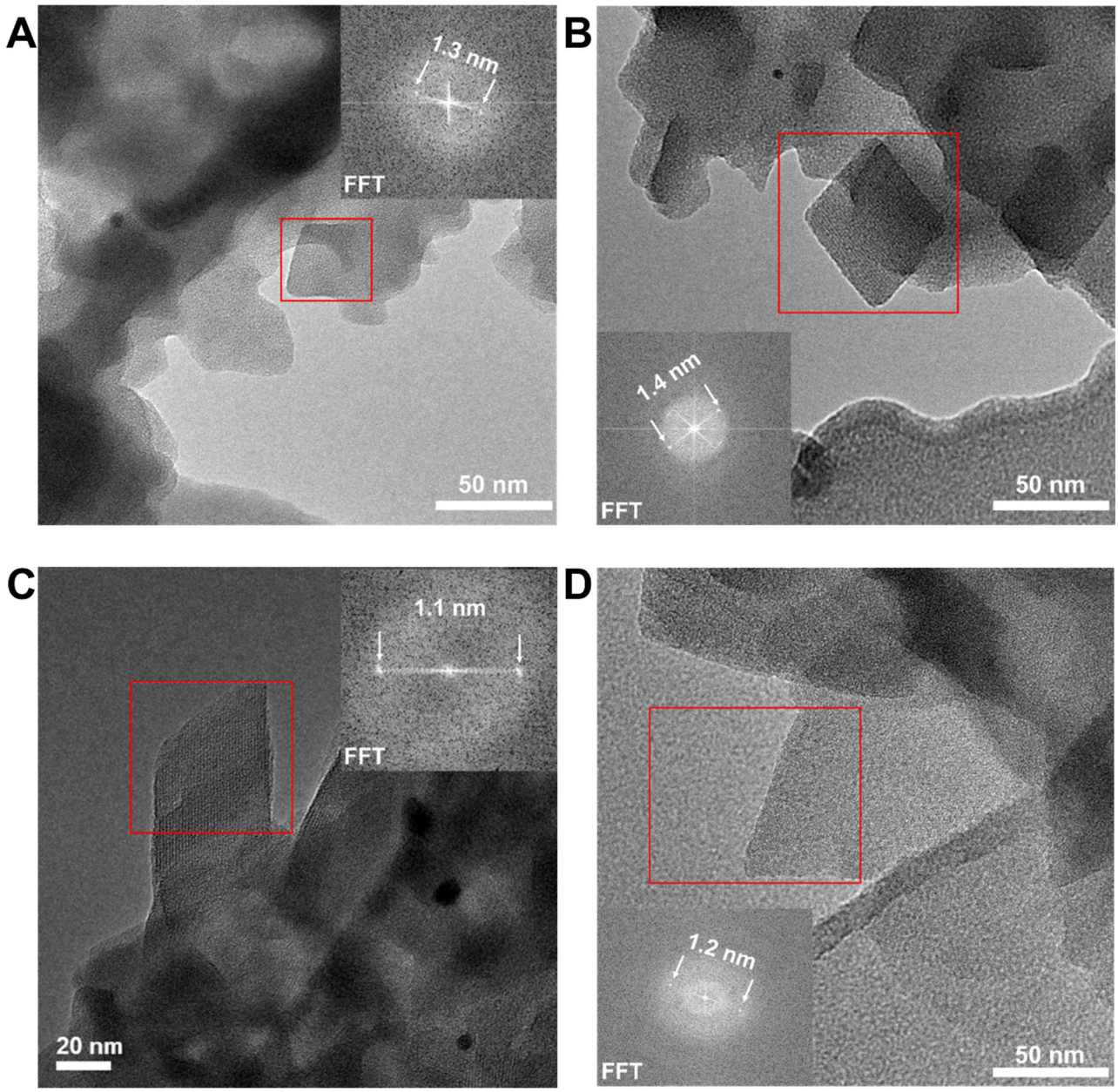

Figure S9. TEM and corresponding FFT images of (A) **1**, (B) **2-Me**, (C) **3**, and (D) **4-Me**, respectively.

Some crystal domains with sharp lattice fringes can be invested by TEM and the spaces by FFT are consistent with d_{110}.

Section S11. TGA curves of 2D [4 + 4] COFs

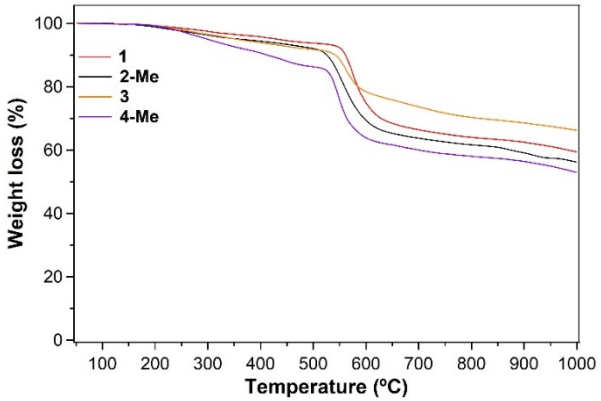

Figure S10. TGA traces for 2D [4 + 4] COFs.

The decomposition of four COFs starts at 200 °C and an obvious stage can be found at 550 °C by TGA, indicating the good thermal stability.

Section S12. Solid state ultraviolet–visible (UV-vis) spectra of 2D [4 + 4] COFs

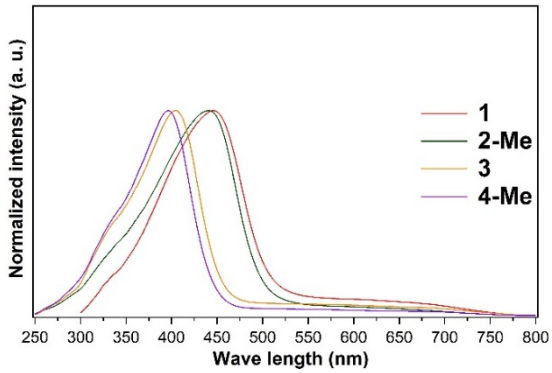

Figure S11. Solid-state UV-vis spectra for 2D [4 + 4] COFs.

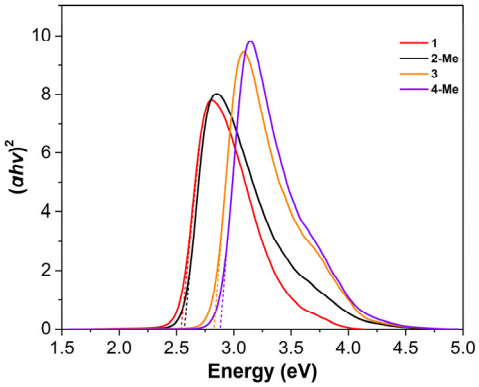

Figure S12. Tauc plots for 2D [4 + 4] COFs.

Compared with **1** and **2-Me**, the blue shifted bands of **3** and **4-Me** by around 50 nm can be ascribed to their lower degree of conjugation. A small blue shift after decorating by methyl groups resulted from the effect of methyl group on delocalization along as well as across the plane in the extended frameworks.

Section S13. BET plots of 2D [4 + 4] COFs

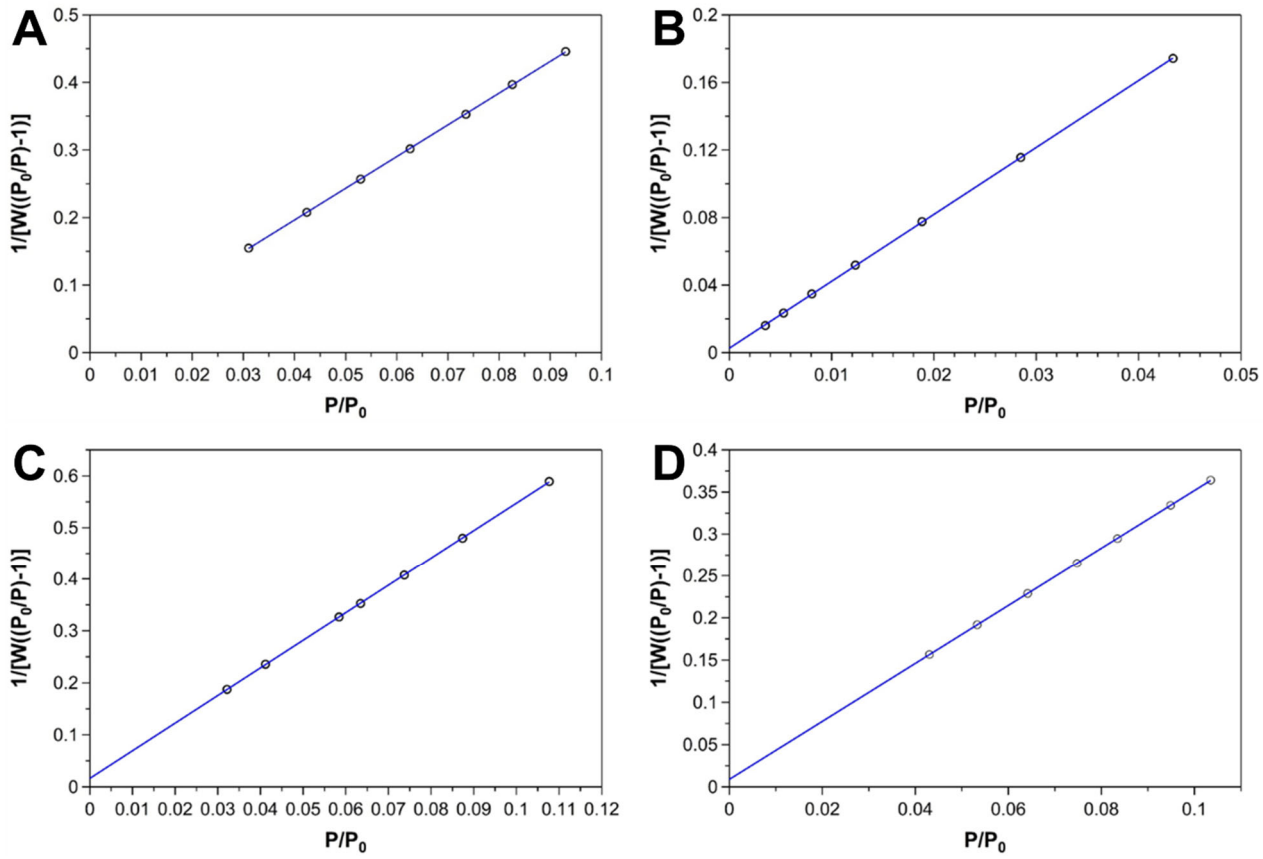

Figure S13. BET plot for (A) **1**, (B) **2-Me**, (C) **3**, and (D) **4-Me**, respectively, calculated from N_2 adsorption data.

The BET plots were simulated by isothermal curves by considering r (correlation coefficient) > 0.99990 and C constant > 0.

Section S14. De Boer *t*-plots of 2D [4 + 4] COFs

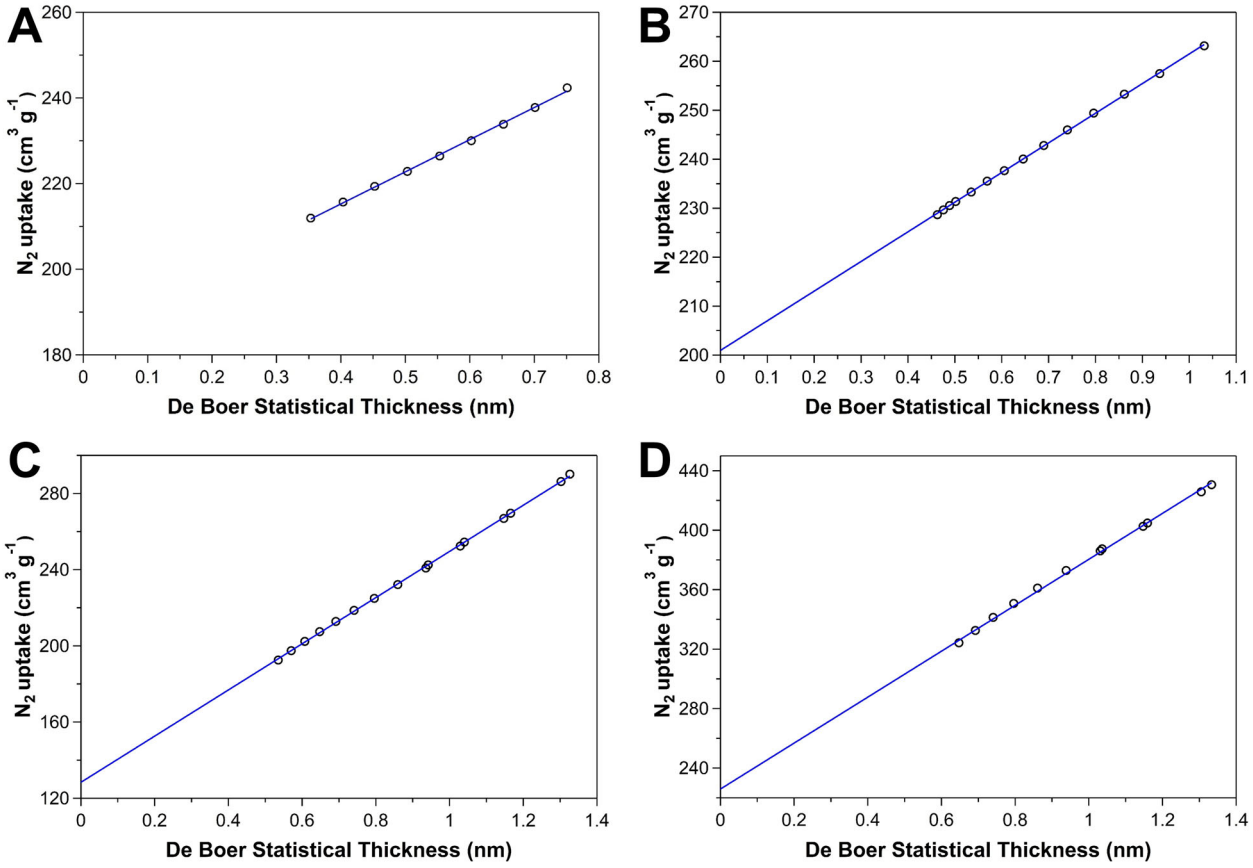

Figure S14. De Boer *t*-plot for (A) **1**, (B) **2-Me**, (C) **3**, and (D) **4-Me**, respectively.

The De Boer *t*-plots by considering r (correlation coefficient) > 0.99990 indicate the micropore contribution is large enough. In addition, the larger micropore contributions of **2-Me** and **4-Me** than those of **1** and **3** suggest the more mesoporous defect might ascribed from the lower polymerization degree of **1** and **3**.

Section S15. Fitting of N_2 isotherms of 2D [4 + 4] COFs

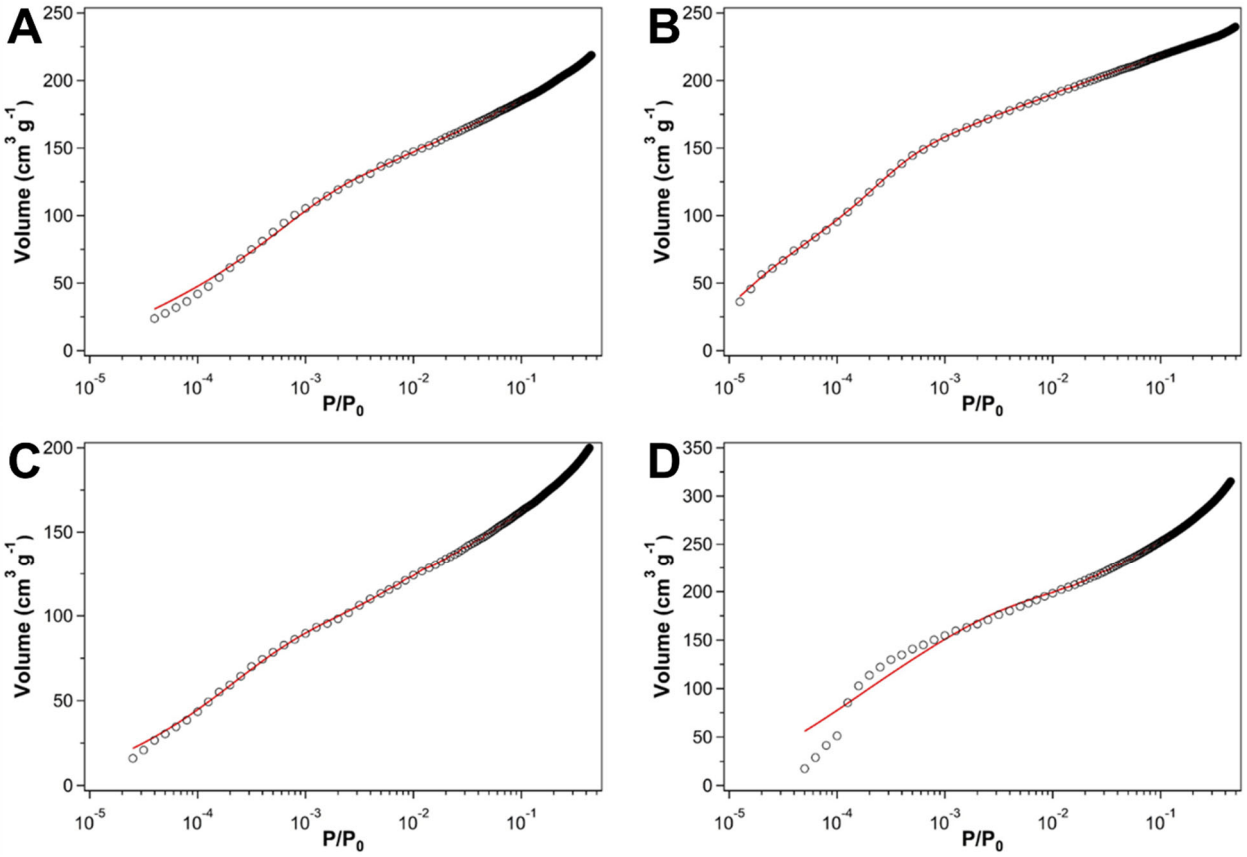

Figure S15. N_2 isotherm (10^{-5}~0.5) for (A) **1**, (B) **2-Me**, (C) **3**, and (D) **4-Me**, respectively, measured at 77 K and used for QSDFT (slit/cylindr./sphere) modeling and pore size distribution calculations.

The fitted adsorption curves with small fitting error indicate QSDFT model is reasonable for simulated pore size distribution.

Section S16. Pore size distribution calculated from N_2 isotherms of 2D [4 + 4] COFs

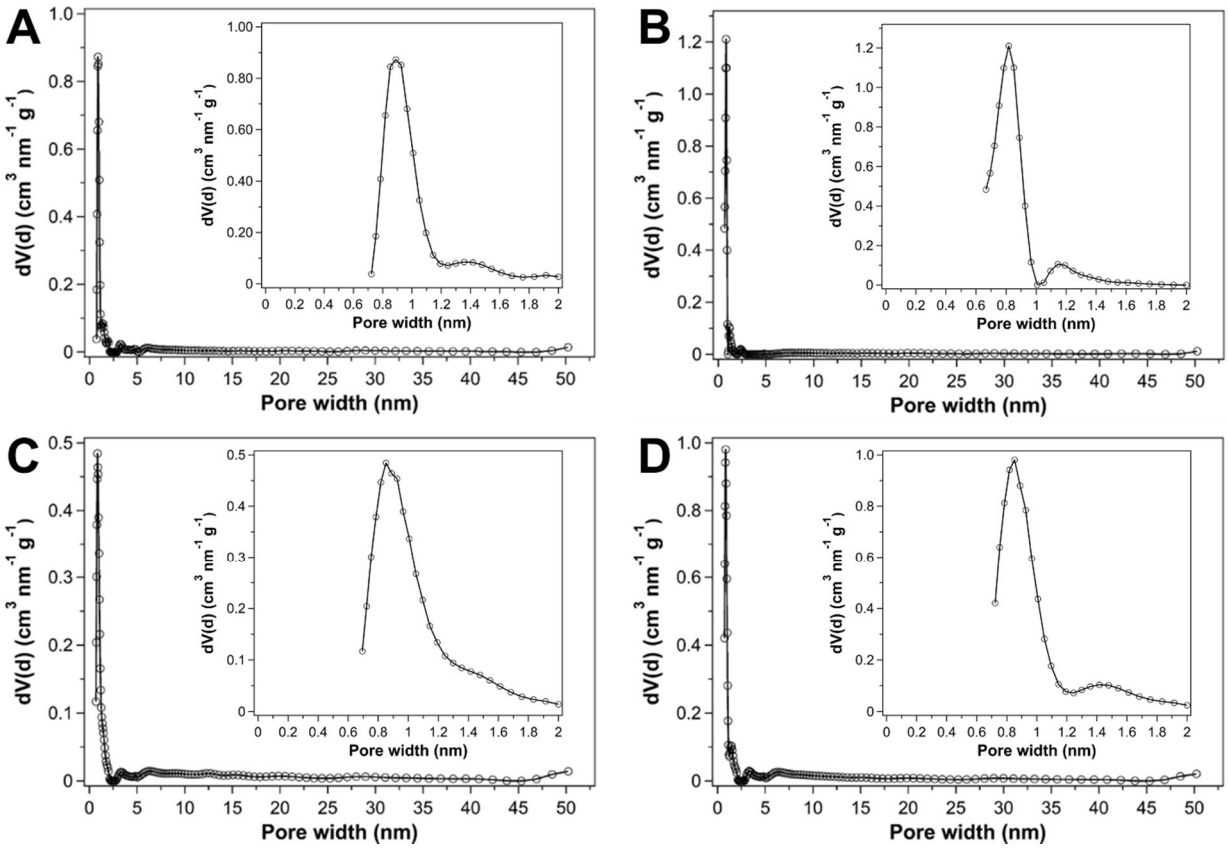

Figure S16. Pore size distribution for (A) **1**, (B) **2-Me**, (C) **3**, and (D) **4-Me**, respectively, calculated after fitting QSDFT (slit/cylindr./sphere) models to N_2 adsorption data (insets are the pore size distribution at the region of 0-2 nm).

The pore size of four COFs all centered range from 0.8~0.9 nm, very close to the theoretical ones.

Section S17. CO_2 and N_2 uptake curves of 2D [4 + 4] COFs

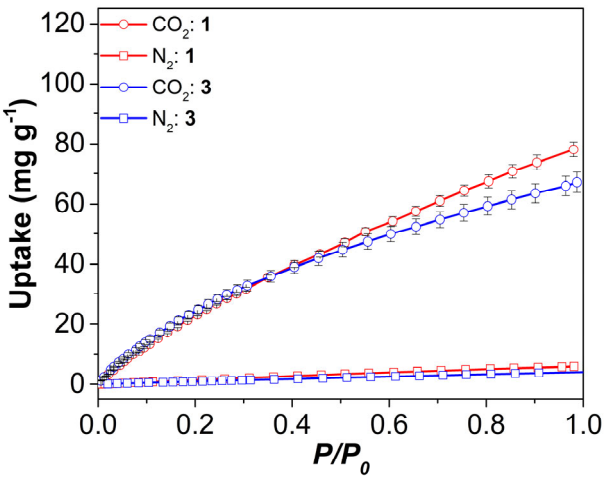

Figure S17. CO_2 and N_2 uptake curves at 273 K for **1** and **3**.

1 and **3** also show a good selectivity towards CO_2 over N_2 (13±0.4 and 16±0.8) owing to the well-defined micropores that hindrance the adsorption of N_2 at 273 K.

Section S18. Cycle performances of 2D [4 + 4] COFs

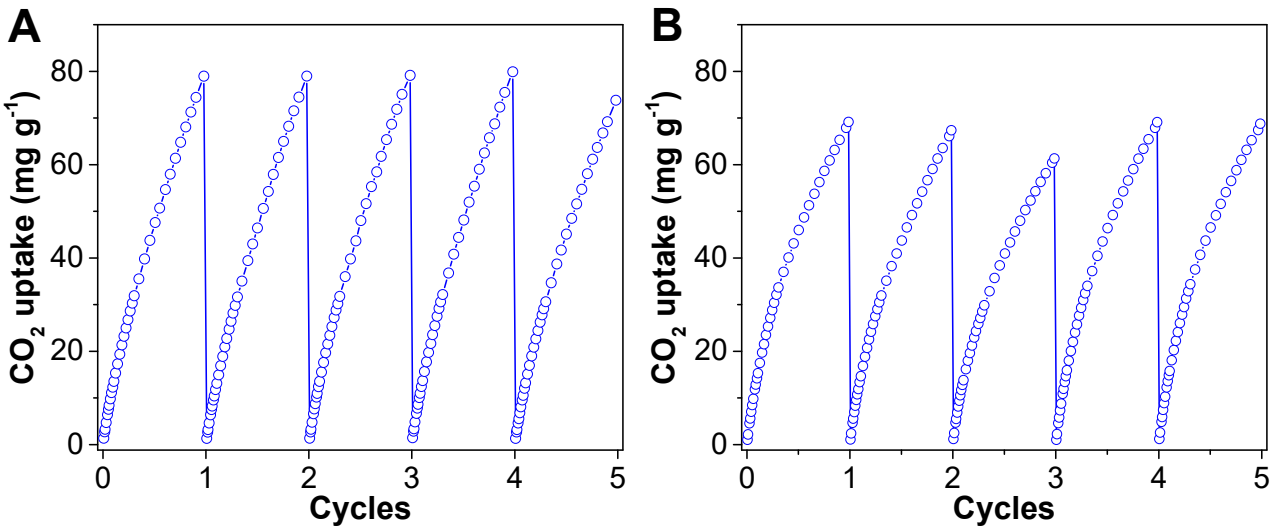

Figure S18. Cycle performances at 273 K of CO_2 uptake for (A) **1** and (B) **3**.

The CO_2 uptakes of four COFs at 273 K do not change obviously after five cycles, indicating the good recyclability of our COFs for CO_2 capture and the interaction between methyl groups and CO_2 is middle and CO_2 can be easily removed from COFs.

Section S19. N_2 isotherms of COF derived N, P co-doped carbons

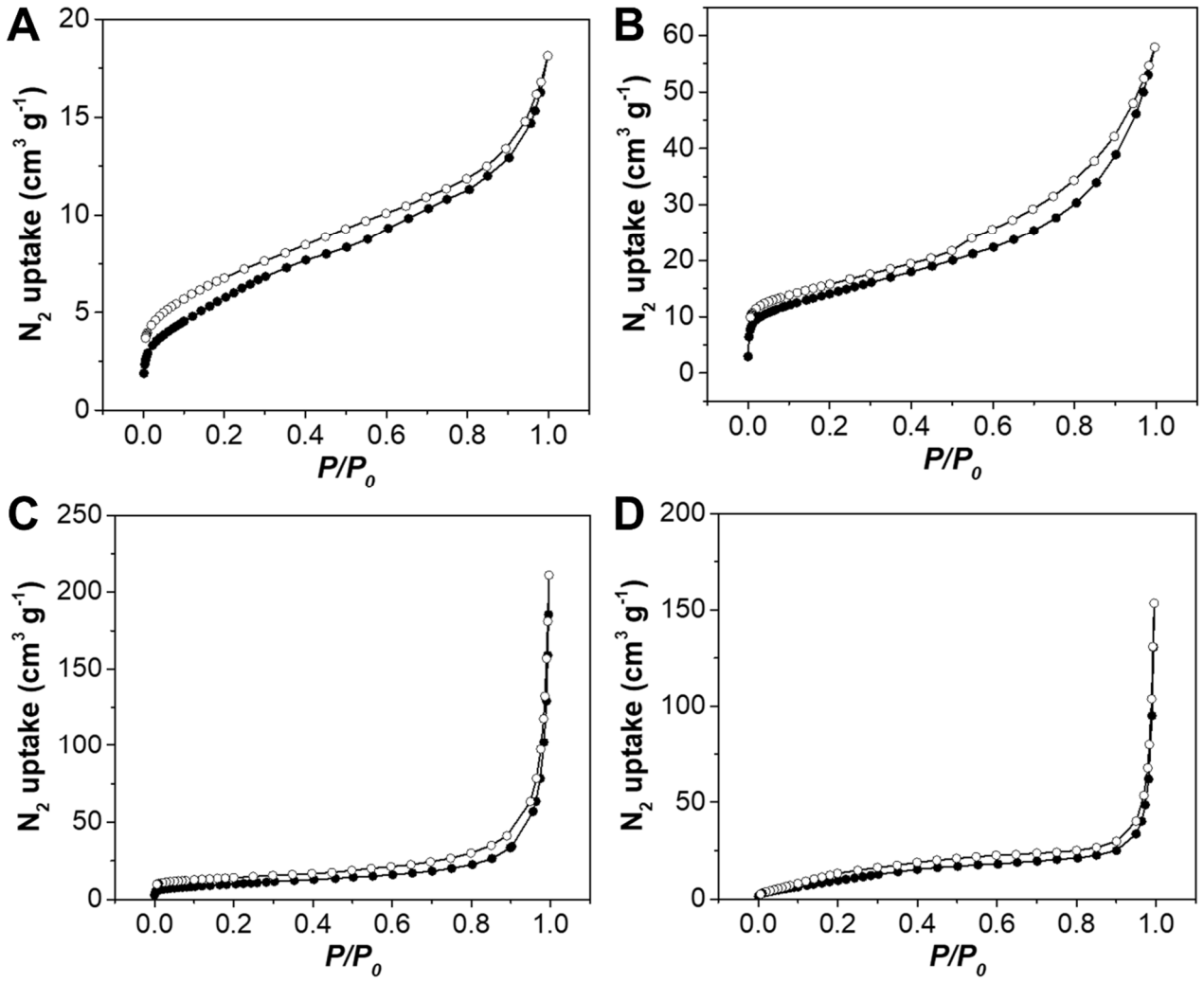

Figure S19. N_2 sorption isotherm of (A) **1”-NP**, (B) **2”-NP**, (C) **3”-NP**, and (D) **4”-NP**, respectively.

N_2 isotherms of **1”-NP** and **2”-NP** (low *P/P₀*: sharp increase, middle/high *P/P₀*: gradual increase) are different from those of **3”-NP** and **4”-NP** (low *P/P₀*: gradual increase, middle *P/P₀*: plateau, high *P/P₀*:sharp increase). The sharp increase of the N_2 uptake in the low pressure region seen in **1”-NP** and **2”-NP** represents existence of micro pores. It suggests that the pore size of the pristine COFs (0.8~0.9 nm, Figure S16) maintains even after carbonization (~1 nm, Figure S20A, B) when the pristine COFs are highly crystalline. In the case of **3”-NP** and **4”-NP**, the N_2 isotherms show sharp increase in the high *P/P₀* region, implying the high outer surface area, often seen nonporous nanomaterials, instead of showing clear sharp increase in the low *P/P₀* region. These results suggest that the low crystalline pristine COFs, **3** and **4-Me** are converted to **3”-NP** and **4”-NP** with inhomogeneous pores (pore distributions show multiple peaks, Figure S20C, D) and small domains (large outer surface).

Section S20. Pore size distribution calculated from N_2 isotherms of COF derived N, P co-doped carbons

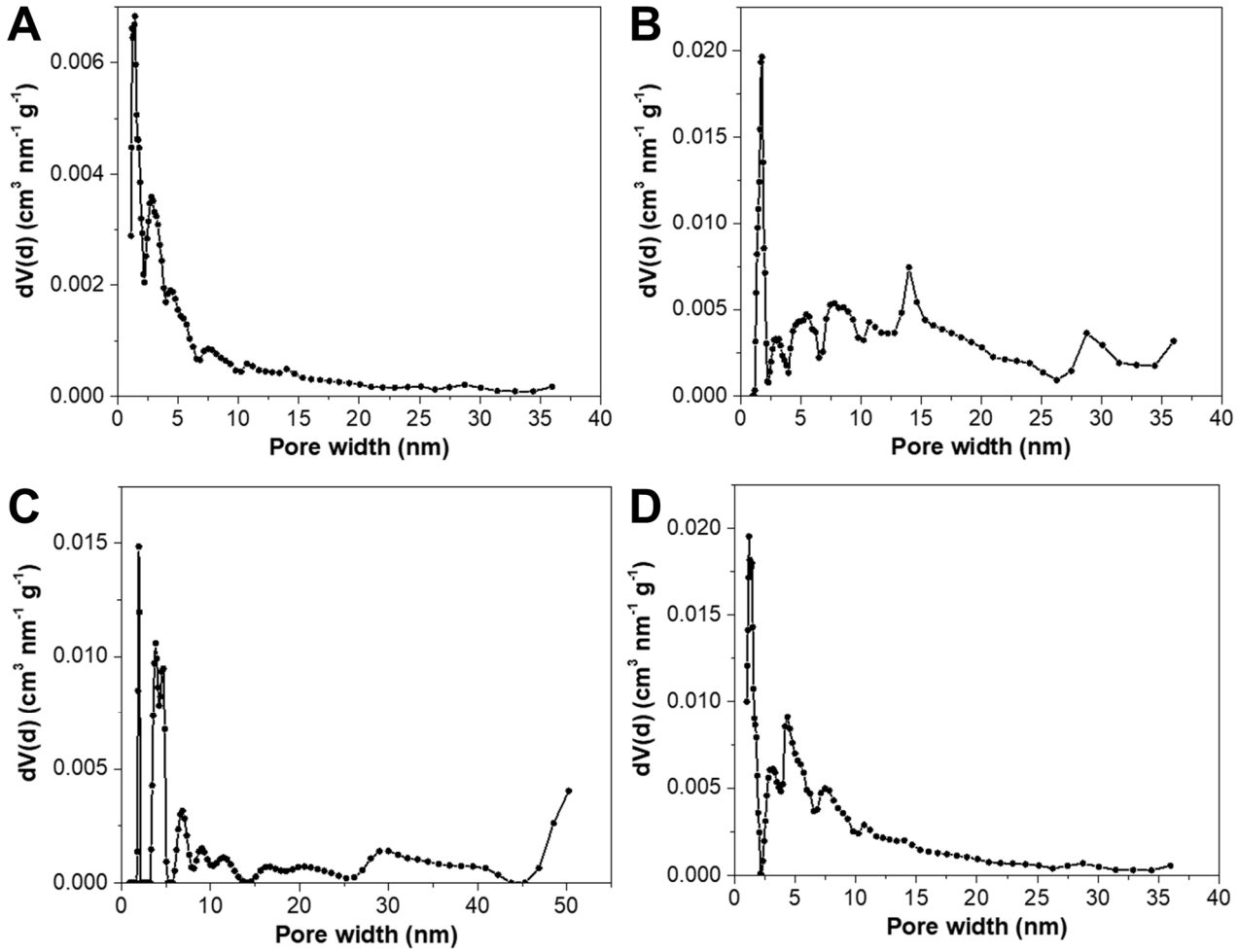

Figure S20. Pore size distribution for (A) **1”-NP**, (B) **2”-NP**, (C) **3”-NP**, and (D) **4”-NP**, respectively, calculated after fitting QSDFT (slit/cylinder/sphere) models to N_2 adsorption data.

Section S21. PXRD patterns of COF derived N, P co-doped carbons

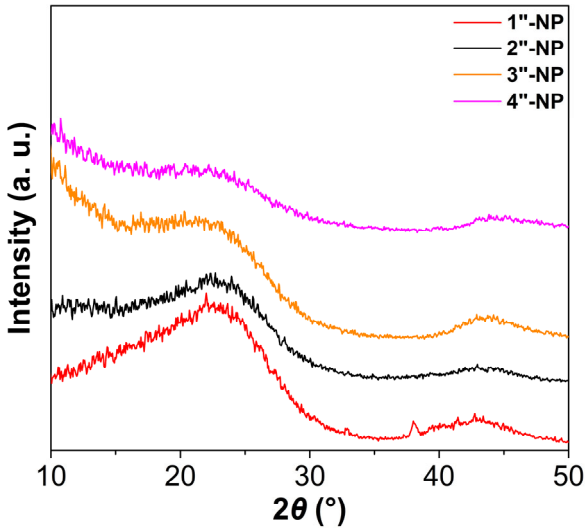

Figure S21. PXRD patterns of COF derived N, P co-doped carbons.

The diffraction peaks at 23° and 43° in PXRD profiles of all four N, P co-doped carbons correspond to the (002) and (100)/(101) facets of graphitized carbon, suggest the transformation of COFs into carbons. the order of the (002) reflection intensity (around 23º) is **1 > 2-Me > 3 ≈ 4-Me** which coincides with the order of the crystallinity in the pristine COFs (**1 > 2-Me > 3 ≈ 4-Me**). High crystallinity of the pristine COFs may contribute to the effective formation of graphitized carbons.

Section S22. Raman spectra of 1'-N and 1"-NP

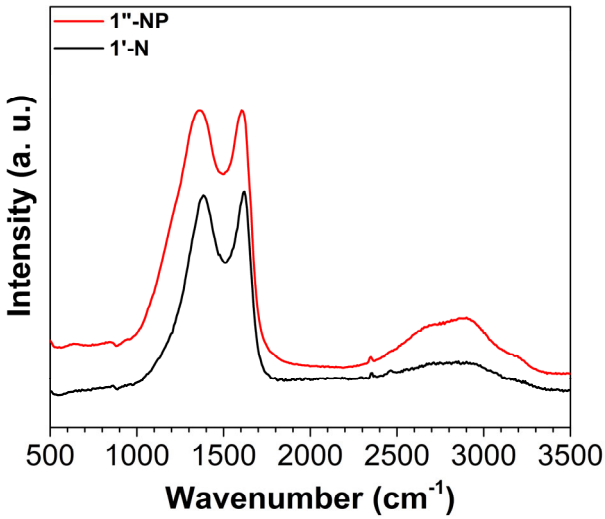

Figure S22. Raman spectra of 1'-N and 1"-NP

Section S23. High-resolution XPS spectra of COF derived N, P co-doped carbons

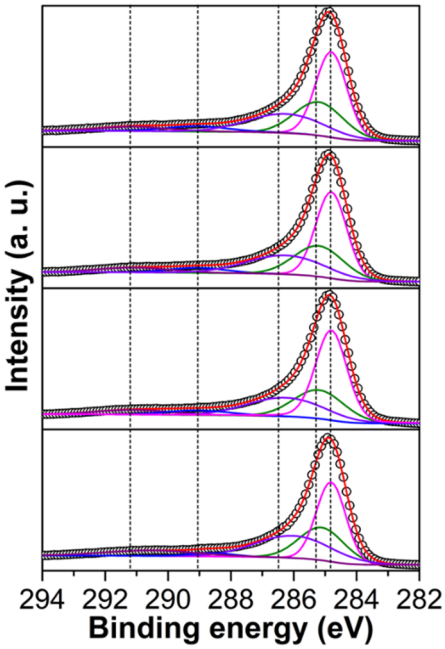

Figure S23. High-resolution XPS spectrum of C 1s of COF derived N, P co-doped carbons (top to bottom: **1”-NP**, **2”-NP**, **3”-NP**, and **4”-NP**, respectively). C-C/C=C: 284.8 eV (pink); C-P: 285.2 eV (green); C-N: 286.3 eV (violet); C-O: 289.1 eV (blue); C=O: 291.1 eV (purple).

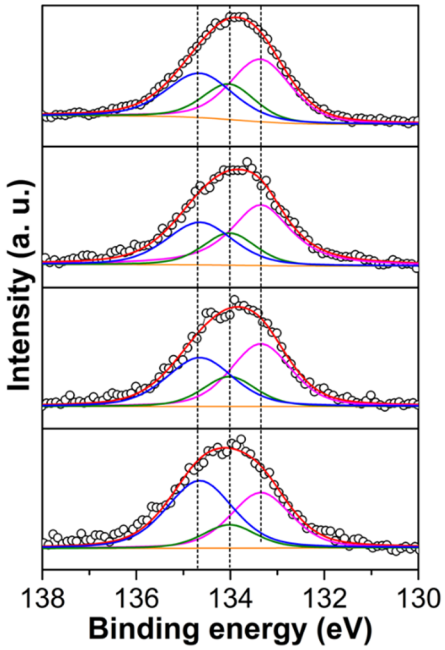

Figure S24. High-resolution XPS spectrum of P 2p of COF derived N, P co-doped carbons (top to bottom: **1”-NP**, **2”-NP**, **3”-NP**, and **4”-NP**, respectively). P-C: 133.4 eV (pink); P-N: 134.0 eV (green); P-O: 134.7 eV (blue).

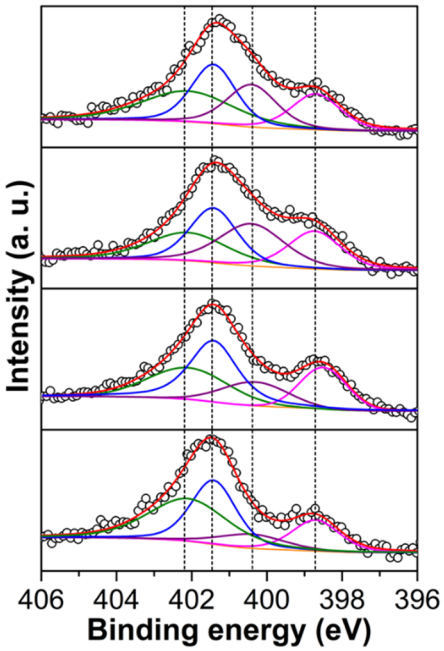

Figure S25. High-resolution XPS spectrum of N 1s of COF derived N, P co-doped carbons (top to bottom: **1”-NP**, **2”-NP**, **3”-NP**, and **4”-NP**, respectively). Pyridinic N: ~398.6 eV (pink); pyrrolic N: 400.4 eV (purple); graphitic N: 401.4 eV (blue); oxidized N: 402.1 eV (green).

XPS C 1s, N 1s and P 2p spectra indicate the successful doping of N, P with graphitic carbon. And the concentrations of various bonds are different due to different structures of COF precursors.

Section S24. Bond concentrations of COF derived N, P co-doped carbons determined by XPS

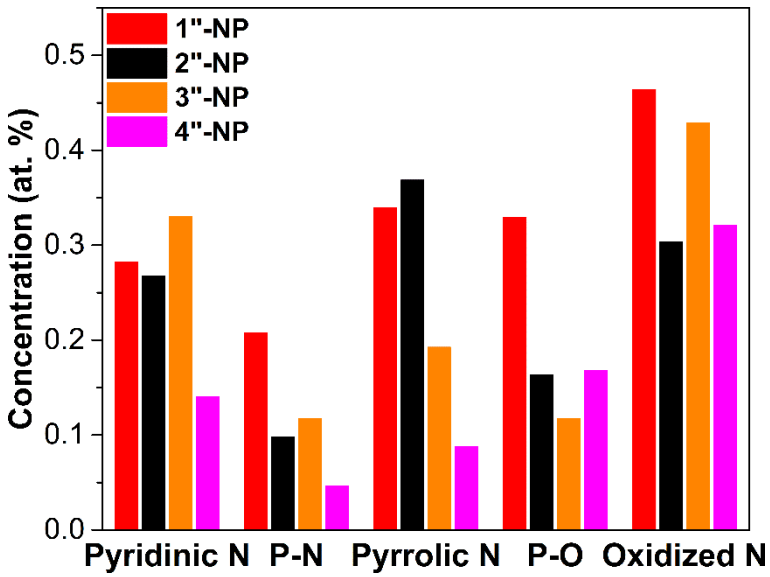

Figure S26. Concentrations of P-N, P-O, pyridinic N, pyrrolic N, and oxidized N based on XPS results for **1”-NP**, **2”-NP**, **3”-NP**, and **4”-NP**.

Section S25. TEM, STEM and EDX mapping images of COF derived N, P co-doped carbons

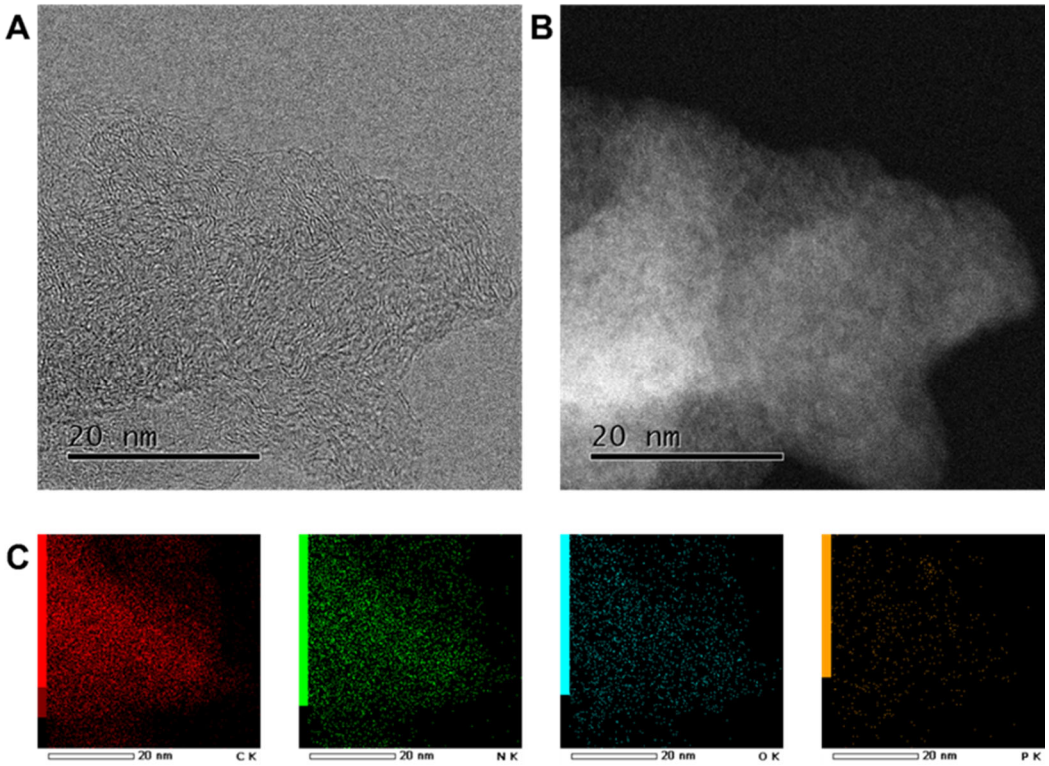

Figure S27. (A) HRTEM image, (B) STEM image and (C) EDS mappings of **1''-NP**.

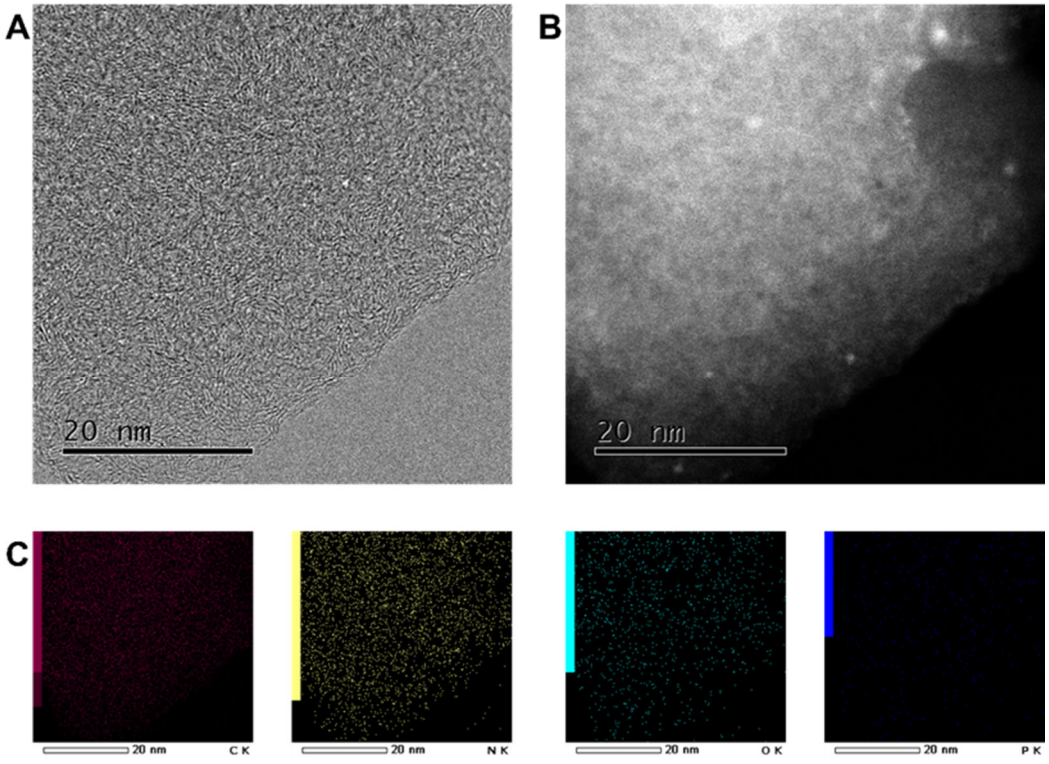

Figure S28. (A) HRTEM image, (B) STEM image and (C) EDS mappings of **2''-NP**.

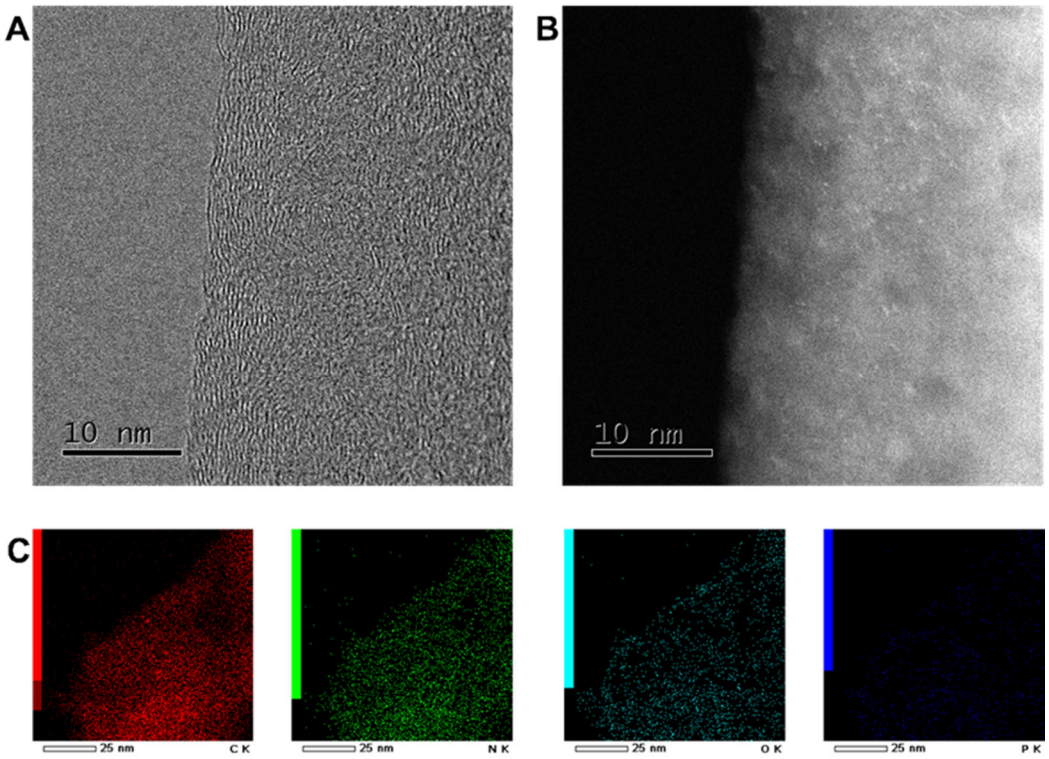

Figure S29. (A) HRTEM image, (B) STEM image and (C) EDS mappings of **3''-NP**.

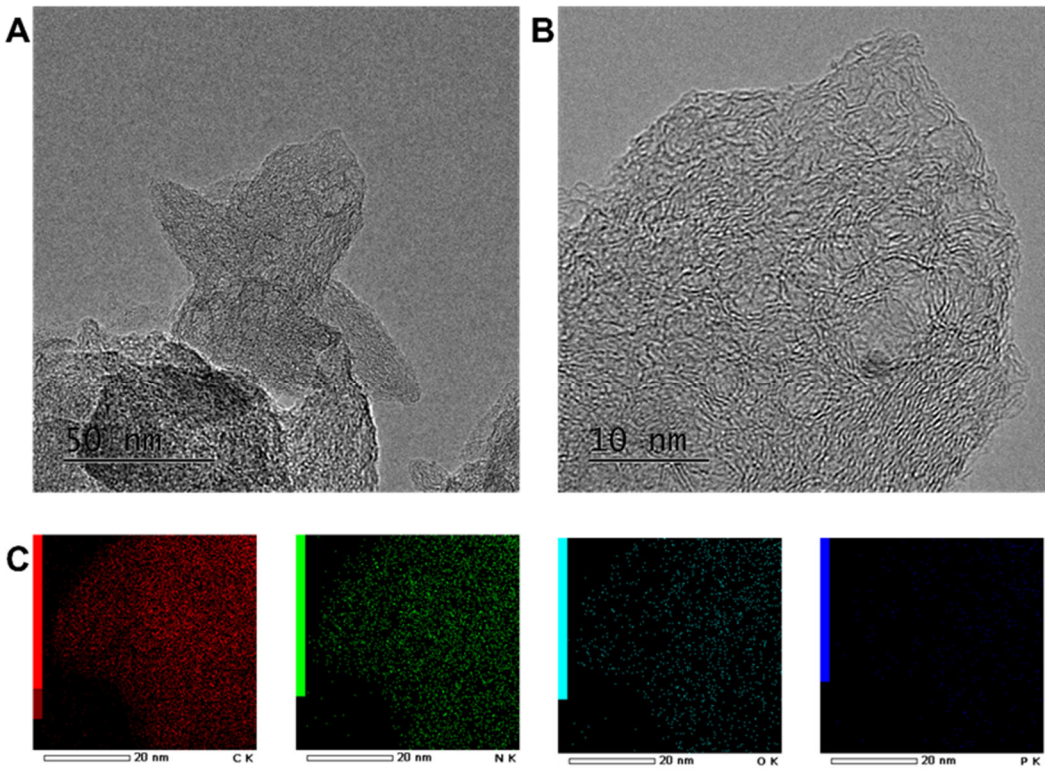

Figure S30. (A) and (B) HRTEM images and (C) EDS mappings of **4''-NP**.

Porous structures and lattice fringe of graphitic carbons can be investigated by TEM. The homogenous signals of C, N, and P by EDS mapping indicate the successful doping of N and P.[6]

Section S26. EIS spectrum of 1”-NP

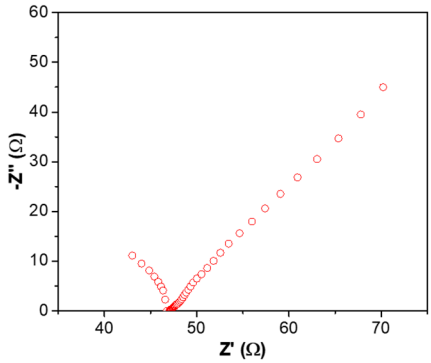

Figure S31. Nyquist plot of **1”-NP** in O_2-saturated 0.10 M KOH solution.

The small charge transfer resistance in electrochemical impedance spectroscopy (EIS) suggests the good ORR performance of **1”-NP**.

Section S27. TEM images of 1”-NP catalyst after a long-term ORR test

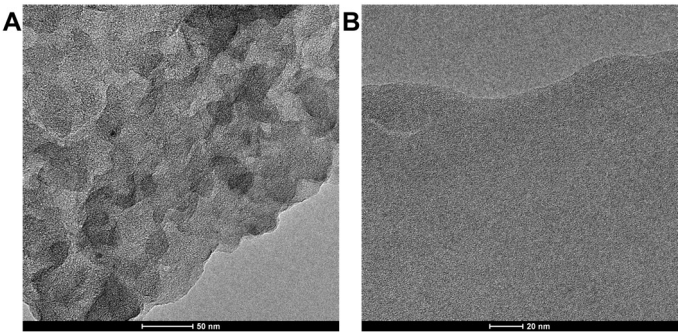

Figure S32. (A) and (B) TEM images of **1”-NP** after a chronoamperometric test over 7 h.

After a long-time test, there is no large structure change in **1”-NP**. The lattice domain of graphitic carbon was hardly investigated by TEM due to the coated Nafion even though the tested sample was washed several times.

Section S28. HER performance

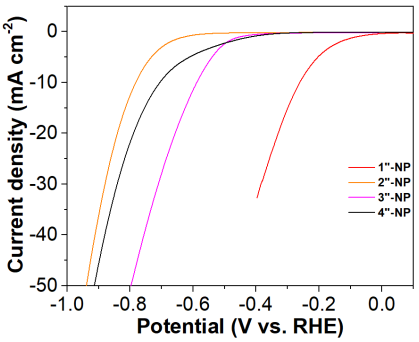

Figure S33. HER plots of **1”-NP**, **2”-NP**, **3”-NP**, and **4”-NP** in Ar-saturated 1.0 M $HClO_4$ solution at a scan rate of 10 mV s^{-1}.

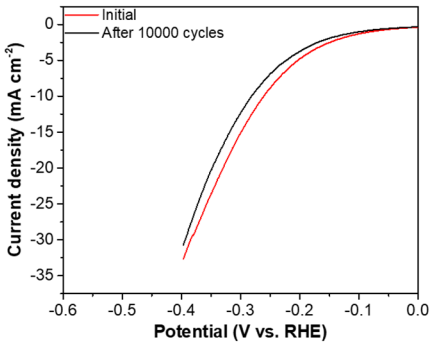

Figure S34. HER plots of **1”-NP** before and after 10000 cycles at a scan rate of 100 mV s^{-1} between -0.2 and 0.2 V vs. RHE. in 1.0 M $HClO_4$ solution.

Compared with the initial, the HER plot after 10000 CV cycles does not change obviously indicating the good stability of 1”-N,P for HER in acid solution.

Section S29. Supporting tables

Table S1. Atom ratios in theory and determined by XPS and elemental analysis

COFs	Theoretical values (C:N:H)	XPS (C:N)	Elemental analysis (C:N:H)
1	15.9 : 1.0 : 0.8	26.4 : 1.0	15.7 : 1.0 : 0.9
2-Me	16.3 : 1.0 : 0.9	18.6 : 1.0	16.6 : 1.0 : 1.0
3	13.7 : 1.0 : 0.7	16.4 : 1.0	14.6 : 1.0 : 0.9
4-Me	14.2 : 1.0 : 0.8	17.4 : 1.0	15.9 : 1.0 : 1.0

Table S2. Porosity parameters and CO_2 capture capacities of selected COFs.

COFs	BET surface area ($m^2\ g^{-1}$)	Pore size (nm)	CO_2 uptake ($mg\ g^{-1}$)	CO_2/N_2 selectivity (w/w)	References
1	741	0.8 - 0.9	78.2±2.5	13±0.4/1	*This work*
2-Me	878	0.8 - 0.9	96.3±3.6	23±0.9/1	*This work*
3	654	0.8 - 0.9	67.1±3.3	16±0.8/1	*This work*
4-Me	1013	0.8 - 0.9	79.5±3.9	30±1.4/1	*This work*
COF-1	750	0.9	100		*7*
COF-5	1670	2.7	60.9		*7*
COF-6	750	0.9	167		*7*
COF-8	1350	1.6	64.8		*7*
COF-10	1760	3.2	53		*7*
COF-102	3620	1.2	66.8		*7*
COF-103	3530	1.2	74.6		*7*
TDCOF-5	2497	2.6	~49		*8*
CTF-1	746	0.54	108	20[a]	*9*
FCTF-1-600	1553	0.46, 0.54	243	31[a]	*9*
TpPa-1	535	1.3	153		*10*
TpPa-2	339	1.4	127		*10*
[HO_2C]100%	364	1.4	174		*11*
TFPB-TAPB-COF	410	1.91	20	5	*12*
TFPA-TAPB-COF	540	1.72	61	13	*12*
BTMA-TAPA-COF	630	1.59	84	16.8	*12*
TFPA-TAPA-COF	660	1.59	105	21	*12*
ACOF-1	1176	0.94	176	10	*13*
N-COF	1700	1.1	120	17	*14*
ILCOF-1	2723	2.3	61		*15*
RT-COF-1	329	1.2	86		*16*
NTU-COF-2	1619	2.5	102		*17*

Table S3. Contents of C, N, and O contents for 2D [4 + 4] COFs determined by XPS

COFs	C (wt. %)	N (wt. %)	O (wt. %)
1	84.89	3.22	11.89
2-Me	92.01	4.95	3.04
3	88.15	5.37	6.48
4-Me	90.36	5.18	4.47

Table S4. Theoretical porosity parameters of 2D [4 + 4] COFs simulated by Poreblazer

COFs	Specific surface area ($m^2\ g^{-1}$)	Pore size (nm)	Accessible surface area ($Å^2$)	Density ($g\ cm^{-3}$)	Cell volume ($Å^3$)
1	1401	0.97	235.91	0.832	2024.49
2-Me	1357	0.93	240.28	0.780	2268.09
3	1520	0.78	224.71	0.783	1887.76
4-Me	1593	0.73	249.24	0.752	2080.26

The flexibility of tetratopic building blocks is poorer than that of linear ones so that the crystallinity of our COFs is lower than those reported COFs. Moreover, since the synthesized COFs are polycrystalline with partial amorphous phase, much lower porosity and crystallinity than expected from the structure models are achieved in our four [4 + 4] COFs.
However, the dense layer structure of 2D COFs enables the dense incorporation of methyl groups onto the well-defined 1D channels without much changing the structure and pore size.

Table S5. Porosities of COF derived N, P co-doped carbons

	Main pore size (nm)
1”-NP	1.1
2”-NP	1.2
3”-NP	1.5
4”-NP	1.9

Table S6. Contents of C, O, N, and P in COF derived N, P co-doped carbons by XPS.

	Contents			
	C (at. %)	N (at. %)	P (at. %)	O (at. %)
1”-NP	89.89	1.50	0.96	7.66
2”-NP	92.70	1.29	0.51	5.49
3”-NP	90.97	1.67	0.31	7.05
4”-NP	93.31	0.82	0.34	5.53

In theory, the N contents followed the sequence of **3** (6.48%)>**4-Me** (6.27%)>**1** (5.66%)>**2-Me** (5.51%). In experiment, the N contents followed the sequence of **3** (5.37%)>**4-Me** (5.18%)>**2-Me** (4.95%)>**1** (3.22%) by XPS and **3** (5.30%)>**4-Me** (4.87%)≈**2-Me** (4.86%)>**1** (4.57%) by elemental analysis. More precisely, the ratio of N/C followed the sequence **3** (1/14.61)>**1** (1/15.72)>**4-Me** (1/15.85)>**2-Me** (1/16.55) by elemental analysis. The experimental result is consistent with the theoretical. The large difference of the defect and amorphous phase between **1** (highest crystallinity) and **4-Me** (lowest crystallinity) might be responsible for the slight fluctuation.

Oxygenated species influence the electrochemical performance. For example, graphene oxides with a lot of oxygen-containing functional groups hardly catalyze electrochemical reactions mainly due to the low conductivity, while reduced graphene oxides exhibit a slight electroactivity after removing the oxygen-containing groups by pyrolysis or hydrothermal reaction (*Nat. Mater.* **2011**, *10*, 780).

As for our doped carbon catalysts, the oxygen contents of all sample are below 8 %, indicating most oxygen-containing groups are removing at high temperature. Therefore, the conductivities of these sample are good enough. The small different content of oxygenated species has not an impact on electroactivity at this level.

Table S7. ORR performance comparison of metal-free and metal-carbon catalysts in O_2-saturated aqueous 0.10 M KOH solutions at a rate constant of 1600 rpm.

Catalysts	Half-wave potential (V)	Limiting current density (mA cm^{-2})	References
1"-NP	0.81 (vs. RHE)	5.5 (at 0.4 V vs. RHE)	*This work*
2"-NP	0.67 (vs. RHE)	3.5 (at 0.4 V vs. RHE)	*This work*
3"-NP	0.68 (vs. RHE)	3.4 (at 0.4 V vs. RHE)	*This work*
4"-NP	0.70 (vs. RHE)	4.7 (at 0.4 V vs. RHE)	*This work*
C-COP-4	0.78 (vs. RHE)	~5.5 (at 0.4 V vs. RHE)	*18*
NPMC-1000	0.85 (vs. RHE)	~4.5 (at 0.4 V vs. RHE)	*19*
PA@TAPT-DHTACOF$_{1000NH3}$	0.87 (vs. RHE)	7.2 (at 0 V vs. RHE)	*20*
MPSA/GO-1000	<0.80 (vs. RHE)	< 5.0 (at 0 V vs. RHE)	*21*
N-S-G	<-0.3 V (vs. Ag/AgCl)		*22*
M-CMP2-800	<-0.14 V (vs. Ag/AgCl)	5.4 (at -0.6 V vs. Ag/AgCl)	*23*
N-HsGDY-900 °C	0.85 (vs. RHE)	6.2 (at 0.2 V vs. RHE)	*24*
h-Mn_3O_4-TMSLs	0.84 (vs. RHE)	5.7 (at 0.2 V vs. RHE)	*25*
Mo–N/C@MoS_2	0.81 (vs. RHE)	5.3 (at 0 V vs. RHE)	*26*
S,N-Fe/N/C-CNT	0.85 (vs. RHE)	6.67 (at 0.2 V vs. RHE)	*27*
Fe-TA-800	<0.80(vs. RHE)	~5.5 (at 0.2 V vs. RHE)	*28*
Co_3O_4/rmGO	0.83 (vs. RHE)	~5.0 (at 0.4V vs. RHE)	*29*
N-CNTs-650	0.85 (vs. RHE)	~5.0 (at 0.4V vs. RHE)	*30*

Table S8. Overpotential (vs. RHE at 10 mA cm^{-2}) comparison of metal-free and metal-carbon catalysts in acid medium.

Catalysts	Overpotential (mV)	References
1''-NP	260 (1.0 M $HClO_4$)	*This work*
MPSA/GO-1000	~200 (0.5 M H_2SO_4)	*21*
1T-MoS_2 sheets	187 (0.5 M H_2SO_4)	*31*
N, P-doped graphene	420 (0.5 M H_2SO_4)	*32*
C_3N_4@N-doped graphene	240 (0.5 M H_2SO_4)	*33*
g-C_3N_4 nanoribbons on graphene sheets	207 (0.5 M H_2SO_4)	*34*
CoP/CNT	226 (0.5 M H_2SO_4)	*35*
NS co-doped graphene 500C	276 (0.5 M H_2SO_4)	*36*

We consider that the two different properties (CO_2 capture and electrocatalysis) are closely related, but in the reverse directions. For example, the CO_2 uptake at 1 atm for **1** (without methyl groups) is 78.2±2.5 mg g^{-1}, while that of **2-Me** (with methyl groups) is 96.3±3.6 mg g^{-1}. On the other hand, in the oxygen reduction reaction (ORR) activities, **1''-NP** (derived from **1**) shows a higher half-wave potential (0.81 V vs. RHE) than that of **2''-NP** (derived from **2-Me**, 0.67 V). This may be attributed to the higher N concentration in **1''-NP** after calcination of **1** while extra methyl groups introduced into **2** decrease the relative contents of N.

References

1. Yang, C. Synthesis and Application of Covalent Organic Frameworks (COFs) and COF Derived Carbons. Ph.D. Thesis, Japan Advanced Institute of Science and Technology, Ishikawa, Japan, **2019**. https://dspace.jaist.ac.jp/dspace/bitstream/10119/16189/2/paper.pdf (accessed 2020-04-30).
2. Bessinger, D.; Ascherl, L.; Auras, F.; Bein, T. Spectrally Switchable Photodetection with Near-Infrared-Absorbing Covalent Organic Frameworks. *J. Am. Chem. Soc.* **2017**, *139*, 12035-12042.
3. Schwab, M. G.; Hamburger, M.; Feng, X.; Shu, J.; Spiess, H. W.; Wang, X.; Antonietti, M.; Müllen, K. Photocatalytic Hydrogen Evolution through Fully Conjugated Poly(azomethine) Networks. *Chem. Commun.* **2010**, *46*, 8932-8937.
4. Altarawneh, S.; Behera, S.; Jena, P.; El-Kaderi, H. M. New Insights into Carbon Dioxide Interactions with Benzimidazole-Linked Polymers. *Chem. Commun.* **2014**, *50*, 3571-3574.
5. Xu, H.; Gao, J.; Jiang, D. Stable, Crystalline, Porous, Covalent Organic Frameworks as a Platform for Chiral Organocatalysts. *Nat. Chem.* **2015**, *7*, 905-912.
6. Qu, K.; Zheng, Y.; Jiao, Y.; Zhang, X.; Dai, S.; Qiao, S. Z. Polydopamine-Inspired, Dual Heteroatom-Doped Carbon Nanotubes for Highly Efficient Overall Water Splitting. *Adv. Energy Mater.* **2017**, *7*, 1602068.
7. Furukawa, H.; Yaghi, O. M. Storage of Hydrogen, Methane, and Carbon Dioxide in Highly Porous Covalent Organic Frameworks for Clean Energy Applications. *J. Am. Chem. Soc.* **2009**, *131*, 8875-8883.
8. Kahveci, Z.; Islamoglu, T.; Shar, G. A.; Ding, R.; El-Kaderi, H. M. Targeted Synthesis of a Mesoporous Triptycene-Derived Covalent Organic Framework. *CrystEngComm* **2013**, *15*, 1524-1527.
9. Zhao, Y.; Yao, K. X.; Teng, B.; Zhang, T.; Han, Y. A Perfluorinated Covalent Triazine-Based Framework for Highly Selective and Water–Tolerant CO_2 Capture. *Energy Environ. Sci.* **2013**, *6*, 3684-3692.
10. Kandambeth, S.; Mallick, A.; Lukose, B.; Mane, M. V.; Heine, T.; Banerjee, R. Construction of Crystalline 2D Covalent Organic Frameworks with Remarkable Chemical (Acid/Base) Stability via a Combined Reversible and Irreversible Route. *J. Am. Chem. Soc.* **2012**, *134*, 19524-19527.

11. Huang, N. Chen, X.; Krishna, R.; Jiang, D. Two-Dimensional Covalent Organic Frameworks for Carbon Dioxide Capture through Channel-Wall Functionalization. *Angew. Chem. Int. Ed.* **2015**, *54*, 2986-2990.

12. Zhai, L.; Huang, N.; Xu, H.; Chen, Q.; Jiang, D. A Backbone Design Principle for Covalent Organic Frameworks: The Impact of Weakly Interacting Units on CO_2 Adsorption. *Chem. Commun.* **2017**, *53*, 4242-4245.

13. Li, Z.; Feng, X.; Zou, Y.; Zhang, Y.; Xia, H.; Liu, X.; Mu, Y. A 2D Azine-Linked Covalent Organic Framework for Gas Storage Applications. *Chem. Commun.* **2014**, *50*, 13825-13828.

14. Gao, Q.; Bai, L.; Zhang, X.; Wang, P.; Li, P.; Zeng, Y.; Zou, R.; Zhao, Y. Synthesis of Microporous Nitrogen-Rich Covalent-Organic Framework and Its Application in CO_2 Capture. *Chin. J. Chem.* **2015**, *33*, 90-94.

15. Rabbani, M. G.; Sekizkardes, A. K.; Kahveci, Z.; Reich, T. E.; Ding, R.; El-Kaderi, H. M. A 2D Mesoporous Imine-Linked Covalent Organic Framework for High Pressure Gas Storage Applications. *Chem. Eur. J.* **2013**, *19*, 3324-3328.

16. de la Pena Ruigomez, A.; Rodriguez-San-Miguel, D.; Stylianou, K. C.; Cavallini, M.; Gentili, D.; Liscio, F.; Milita, S. Roscioni, O. M.; Ruiz-Gonzalez, M. L.; Carbonell, C.; Maspoch, D.; Mas-Balleste, R.; Segura, J. L.; Zamora, F. Direct On-Surface Patterning of a Crystalline Laminar Covalent Organic Framework Synthesized at Room Temperature. *Chem. Eur. J.* **2015**, *21*, 10666-10670.

17. Zeng, Y.; Zou, R.; Luo, Z.; Zhang, H.; Yao, X.; Ma, X.; Zou, R.; Zhao, Y. Covalent Organic Frameworks Formed with Two Types of Covalent Bonds Based on Orthogonal Reactions. *J. Am. Chem. Soc.* **2015**, *137*, 1020-1023.

18. Xiang, Z.; Cao, D.; Huang, L.; Shui, J.; Wang, M.; Dai, L. Nitrogen-Doped Holey Graphitic Carbon from 2D Covalent Organic Polymers for Oxygen Reduction. *Adv. Mater.* **2014**, *26*, 3315-3320.

19. Zhang, J.; Zhao, Z.; Xia, Z.: Dai, L. A Metal-Free Bifunctional Electrocatalyst for Oxygen Reduction and Oxygen Evolution Reactions. *Nat. Nanotechnol.* **2015**, *10*, 444-452.

20. Xu, Q.; Tang, Y.; Zhang, X.; Oshima, Y.; Chen, Q.; Jiang, D. Template Conversion of Covalent Organic Frameworks into 2D Conducting Nanocarbons for Catalyzing Oxygen Reduction Reaction. *Adv. Mater.* **2018**, *30*, 1706330.

21. Zhang, J.; Qu, L.; Shi, G.; Liu, J.; Chen, J.; Dai, L. N, P-Codoped Carbon Networks as Efficient Metal-Free Bifunctional Catalysts for Oxygen Reduction and Hydrogen Evolution Reactions. *Angew. Chem. Int. Ed.* **2016**, *55*, 2230-2234.

22. Liang, J.; Jiao, Y.; Jaroniec, M.; Qiao, S. Z. Sulfur and Nitrogen Dual-Doped Mesoporous Graphene Electrocatalyst for Oxygen Reduction with Synergistically Enhanced Performance. *Angew. Chem. Int. Ed.* **2012**, *51*, 11496-11500.

23. Yuan, K.; Zhuang, X.; Fu, H.; Brunklaus, G.; Forster, M.; Chen, Y.; Feng, X.; Scherf, U. Two-Dimensional Core-Shelled Porous Hybrids as Highly Efficient Catalysts for the Oxygen Reduction Reaction. *Angew. Chem. Int. Ed.* **2016**, *55*, 6858-6863.

24. Lv, Q.; Si, W.; He, J.; Sun, L.; Zhang, C.; Wang, N.; Yang, Z.; Li, X.; Wang, X.; Deng, W.; Long, Y.; Huang C.; Li, Y. Selectively Nitrogen-Doped Carbon Materials as Superior Metal-Free Catalysts for Oxygen Reduction. *Nat. Commun.* **2018**, *9*, 3376.

25. Li, T.; Xue, B.; Wang, B.; Guo, G.; Han, D.; Yan, Y.; Dong, A. Tubular Monolayer Superlattices of Hollow Mn_3O_4 Nanocrystals and Their Oxygen Reduction Activity. *J. Am. Chem. Soc.* **2017**, *139*, 12133-12136.

26. Amiinu, I. S.; Pu, Z.; Liu, X.; Owusu, K. A.; Monestel, H. G. R.; Boakye, F. O.; Zhang, H.; Mu, S. Multifunctional Mo–N/C@MoS_2 Electrocatalysts for HER, OER, ORR, and Zn–Air Batteries. *Adv. Funct. Mater.* **2017**, *27*, 1702300.

27. Chen, P.; Zhou, T.; Xing, L.; Xu, K.; Tong, Y.; Xie, H.; Zhang L; Yan, W.; Chu W.; Wu, C.; Xie, Y. Atomically Dispersed Iron–Nitrogen Species as Electrocatalysts for Bifunctional Oxygen Evolution and Reduction Reactions. *Angew. Chem. Int. Ed.* **2017**, *56*, 610-614.

28. Wei, J.; Liang, Y.; Hu, Y.; Kong, B.; Zhang, J.; Gu, Q.; Tong, Y.; Wang, X.; Jiang, S. P.; Wang, H. Hydrothermal Synthesis of Metal–Polyphenol Coordination Crystals and Their Derived Metal/N-doped Carbon Composites for Oxygen Electrocatalysis. *Angew. Chem. Int. Ed.* **2016**, *55*, 12470-12474.

29. Liang, Y.; Li, Y.; Wang, H.; Zhou, J.; Wang, J.; Regier, T.; Dai, H. Co_3O_4 Nanocrystals on Graphene as a Synergistic Catalyst for Oxygen Reduction Reaction. *Nat. Mater.* **2011**, *10*, 780-786.

30. Meng, J.; Niu, C.; Xu, L.; Li, J.; Liu, X.; Wang, X.; Wu, Y.; Xu, X.; Chen, W.; Li, Q.; Zhu, Z.; Zhao, D.; Mai, L. General Oriented Formation of Carbon Nanotubes from Metal–Organic Frameworks. *J. Am. Chem. Soc.* **2017***, 139,* 8212-8221.

31. Lukowski, M. A.; Daniel, A. S.; Meng, F.; Forticaux, A.; Li, L.; Jin, S. Enhanced Hydrogen Evolution Catalysis from Chemically Exfoliated Metallic MoS_2 Nanosheets. *J. Am. Chem. Soc.* **2013**, *135*, 10274-10277.

32. Zheng, Y.; Jiao, Y.; Li, L. H.; Xing, T.; Chen, Y.; Jaroniec, M.; Qiao, S. Z. Toward Design of Synergistically Active Carbon-Based Catalysts for Electrocatalytic Hydrogen Evolution. *ACS Nano* **2014**, *8*, 5290-5296.

33. Zheng, Y.; Jiao, Y.; Zhu, Y.; Li, L. H.; Han, Y.; Chen, Y.; Du, A.; Jaroniec M.; Qiao, S. Z. Hydrogen Evolution by a Metal-Free Electrocatalyst. *Nat. Commun.* **2014**, *5*, 3783.

34. Zhao, Y.; Zhao, F.; Wang, X.; Xu, C.; Zhang, Z.; Shi, G.; Qu, L. Graphitic Carbon Nitride Nanoribbons: Graphene‐Assisted Formation and Synergic Function for Highly Efficient Hydrogen Evolution. *Angew. Chem. Int. Ed.* **2014**, *53*, 13934-13939.

35. Liu, Q.; Tian, J.; Cui, W.; Jiang, P.; Cheng, N.; Asiri, A. M.; Sun, X. Carbon Nanotubes Decorated with CoP Nanocrystals: A Highly Active Non-Noble-Metal Nanohybrid Electrocatalyst for Hydrogen Evolution. *Angew. Chem. Int. Ed.* **2014**, *53*, 6710-6714.

36. Ito, Y.; Cong, W.; Fujita, T.; Tang, Z.; Chen, M. High Catalytic Activity of Nitrogen and Sulfur Co-doped Nanoporous Graphene in the Hydrogen Evolution Reaction. *Angew. Chem. Int. Ed.* **2015**, *54*, 2131-2136.